ABSTRACT

RICHARDSON, HEATHER LYNN. Improving Stable Boundary Layer Parameterization in a Mesoscale Model to Better Represent Nocturnal Low-Level Jets. (Under the direction of Sukanta Basu.)

A low-Level jet (LLJ) is a wind speed maximum that typically occurs between 100-1000m above ground level (AGL). They are common throughout the globe, affecting many different societies. One location where LLJs are predominantly found is the United States Great Plains (USGP). Since LLJs are areas of high wind speed concentration, they are great resources of wind energy. As a consequence, areas like the USGP have witnessed a boom in the development of wind farms across the region. Although LLJs can be a great resource for wind, they can also cause damages to wind turbines through increase in wind shear (change in wind speed/direction with height).

Given that LLJs have both positive and negative consequences in the wind energy community, it is imperative that they be simulated and forecasted with great accuracy and minimal uncertainty. Unfortunately, contemporary mesoscale models have not been very successful in accomplishing these tasks. Since mesoscale models heavily rely on the planetary boundary layer (PBL) parameterization schemes to represent PBL physics and dynamics, one needs to improve the PBL schemes for better representation of the LLJs. This thesis attempts to contribute in this scientific arena.

The critical bulk Richardson number is a key ingredient of many PBL parameterizations. In this thesis, a new formulation for critical bulk Richardson number is found and a modified PBL scheme is proposed. The strengths and weaknesses of this new scheme are explored by conducting several single column model and mesoscale simulations.

Improving Stable Boundary Layer Parameterization in a Mesoscale Model to Better Represent Nocturnal Low-Level Jets

by
Heather Lynn Richardson

A thesis submitted to the Graduate Faculty of
North Carolina State University
in partial fulfillment of the
requirements for the Degree of
Master of Science

Marine, Earth, and Atmospheric Sciences

Raleigh, North Carolina

2012

APPROVED BY:

Sandra Yuter	Matthew Parker
Neil Jacobs	Sukanta Basu Chair of Advisory Committee

DEDICATION

This thesis is lovingly dedicated to my husband, who has supported me every step of the way. Also, this thesis is dedicated to our parents for their never ending financial and moral support.

BIOGRAPHY

Heather Richardson was the second child of Francis and Robin Russett born in San Diego, CA. With her father employed by the United States Navy, moving to new and different states was not uncommon until his retirement. At 11 years of age her family settled in Winston-Salem, NC where she went on to graduate high school with honors in May 2006.

In the fall of 2006 she enrolled at North Carolina State University in pursuit of a Bachelor's Degree in Meteorology. In the following four years she took advantage of several different opportunities while obtaining the dean's list for several semesters. For the summer of 2008 she attended an internship with the WXII news channel 12 weather team learning broadcasting skills. The following January in 2009 she started working at the North Carolina State Climate Office performing model evaluation until the end of the summer in 2010. In June of 2010 she obtained her bachelor's degree in meteorology with honors.

Shortly after finishing at the North Carolina State Climate Office she continued her academic career and started pursuing her Master's Degree in Atmospheric Science in the fall of 2010. For the summer of 2011 she attended the Weather Research and Forecasting (WRF) conference in Boulder, CO as well as interned at Airdat LLC. During her two years at North Carolina State University between 2010 and 2012 she will earn her degree in atmospheric sciences under the direction of Dr. Sukanta Basu. Upon finishing her degree she will begin working full time at Airdat LLC.

ACKNOWLEDGEMENTS

This work was partially supported by the National Science Foundation (AGS-1122315) grant.

I owe my deepest gratitude to my advisor Dr. Sukanta Basu for all of his support, encouragment and guidance from the beginning to the end. His patience and motiviation helped me through some of my most trying times and was a major factor in the completion of this thesis.

It is an honor for me to also thank all of my committee members Dr. Neil Jacobs, Dr. Matthew Parker and Dr. Sandra Yuter. All of their insightful comments and advice were an integral part of my research and in developing this thesis.

I am also indebted to the members of the North Carolina State University boundary layer meteorology group with whom I have interacted during the course of my graduate studies. A special gratitude is sent to Jeffery Craft, Velayudhan Praju Kiliyanpilakkil, Christopher Nunalee and Yao Wang for all their constructive criticisms and moral support. Their never ending encouragment is something I will never forget.

TABLE OF CONTENTS

LIST OF TABLES

LIST OF FIGURES

Chapter 1

Introduction

In today's global market both government and business sectors alike are becoming less dependent on fossil fuel sources and more dependent on renewable energies. This transitional push stems from recent issues surrounding climate change and the need for more reliable and economical energy resources to sustain the world's ever increasing need for power. Within the arena of renewable energy the fastest growing sector is wind energy. Wind is a highly attractive source of energy because it is relatively inexpensive, clean, and is available worldwide. Since wind is such an abundant resource, the absence of wind turbines essentially signifies a loss of energy and revenue.

The desirability of the wind energy source has caused a boom in its development during the last decade with the installed global capacity increasing at exponential rates. For example, in the United States (henceforth US), according to the National Renewable Energy Laboratory (NREL), the wind power capacity has increased from 2,539 MW to 46,919 MW during the years 2000-2011 (see Figure 1.1). This trend is expected to continue in the coming decades [DOE, 2008].

In the US, most of the wind farms have been installed in the Great Plains region (henceforth, USGP; see left panel of Figure 1.2). In this region of the world an atmospheric phenomenon known as the nocturnal low-level jet (LLJ) is known to develop quite frequently. LLJs are typically defined as wind speed maxima with the core developing around 100-1000m above ground level (AGL). These LLJs are excellent sources for energy/power and it is no coincidence that large investments (billions of dollars) have been made for wind energy production in the USGP where LLJs are prevalent. The right panel of Figure 1.2 illustrates the available wind resources in the United States at 80m AGL; The USGP has relatively high available resources.

Although LLJs are a great source of wind energy, they can present unique challenges for wind turbines. Increased vertical wind shear (difference of wind speed/direction with height) at the approximate level of turbine hub heights can be observed within LLJs [Kelley et al.,

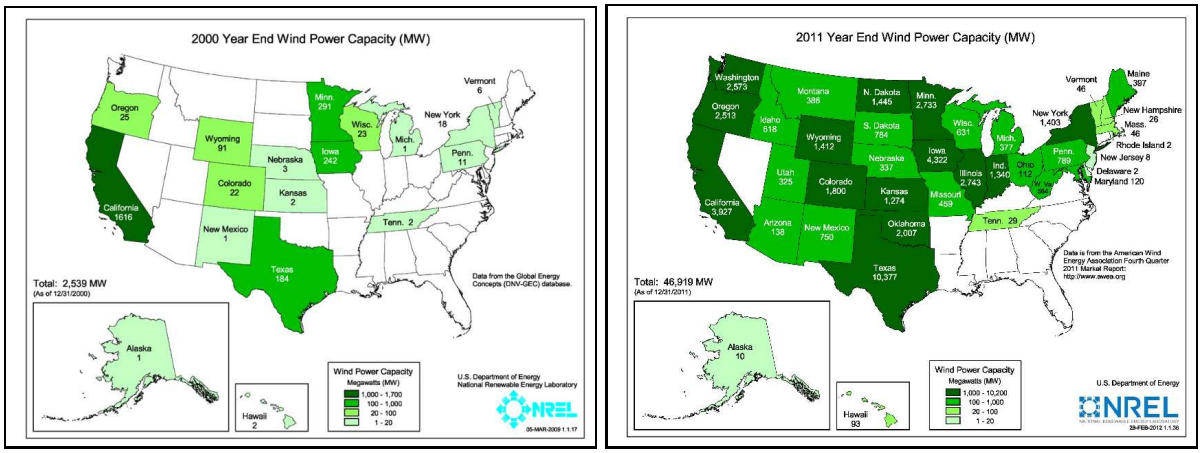

Figure 1.1: US wind power capacity in the years 2000 (left-panel) and 2011 (right-panel) (http://www.windpoweringamerica.gov/wind_installed_capacity.asp)

.

2004]. A high level of shear (and associated turbulence) over the turbine rotor plane can cause unsteady loads on the blades which may eventually lead to fatigue damage and turbine failure. Key turbine parts and terminologies, such as turbine rotor plane, are depicted in figure 1.3.

About a decade ago, Banta et al. [2002] noted that the numerical weather prediction (NWP) models have limited capabilities in reliably simulating LLJs. This situation has not improved as evident from the recent literature including (but not limited to): Storm and Basu [2010], Shin and Hong [2011], Russett and Basu [2011], and Richardson et al. [2012]. These studies investigated the performance of a new-generation mesoscale model, the Weather Research and Forecasting (WRF) model, in simulating LLJs over the USGP. All of these studies utilized several planetary boundary layer (PBL) schemes (with varying orders of turbulent closure) and reported that a widely used first-order PBL scheme, called the Yonsei University (YSU) scheme [Hong et al., 2006, Hong, 2010], performed rather poorly. This PBL scheme produced excessive turbulent mixing during the nighttime hours (i.e., stably stratified conditions) and led to deeper and weaker LLJs than observed. The poorer performance of the YSU scheme in comparison to other higher-order schemes deserves further investigation for the following reasons:

- the YSU scheme is widely used by operational forecasting centers (e.g., at the National Center for Atmospheric Research – NCAR) and various industries (e.g., AWS Truepower);
- in the spirit of the well-known Occam's razor principle, a simple parameterization (such as the YSU scheme) is always more desirable than a complex one (e.g., a second or a third-order scheme), if both demonstrate more-or-less comparable performances; and
- The YSU scheme utilizes the K-profile approach which is theoretically consistent with

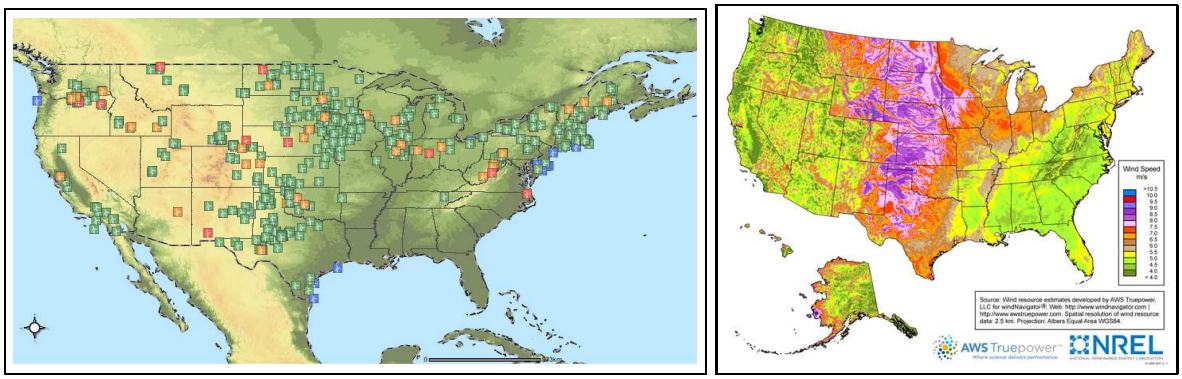

Figure 1.2: Left panel: Wind farms in the US (http://windenergy.ornl.gov/gis). Right panel: US wind resource map at 80 m AGL
(http://www.windpoweringamerica.gov/wind_maps_none.asp).

Nieuwstadt's local scaling hypothesis [Nieuwstadt, 1984].[1]

In this thesis, such an investigation is pursued to address the following scientific questions:

- Why do first-order closure schemes (e.g., the YSU scheme) perform poorly in nocturnal LLJ simulations?
- Can the performance of these schemes be improved by incorporating novel boundary layer concepts?

Specifically, the objectives of this thesis research are:

- to develop improved (or to amend the existing) first-order PBL scheme(s) for reliable simulations of nocturnal low-level jets; and
- to investigate the performance of the newly proposed as well as the existing PBL scheme(s) in single column and mesoscale models.

For an improvement to take place with the first-order PBL schemes, their simulations of LLJs need to increase the core wind speed magnitude and decrease the LLJ height. The overall hypothesis driving the objectives of this research is that the enhanced mixing is caused by an issue with the boundary layer height parameterization. With boundary layer height being a major player in the eddy diffusivity equation (revealed later) it would make sense that improving this parameterization would enhance the performance of the YSU PBL scheme.

The structure of this thesis is as follows. In Chapter 2, some background materials on stable boundary layers (common developmental regime of LLJs) and LLJs are provided. Also in this

[1]Basu et al. [2006] analyzed data from field observations, wind tunnel experiments, and large-eddy simulations and found the local scaling hypothesis to be valid for a wide range of stably stratified conditions.

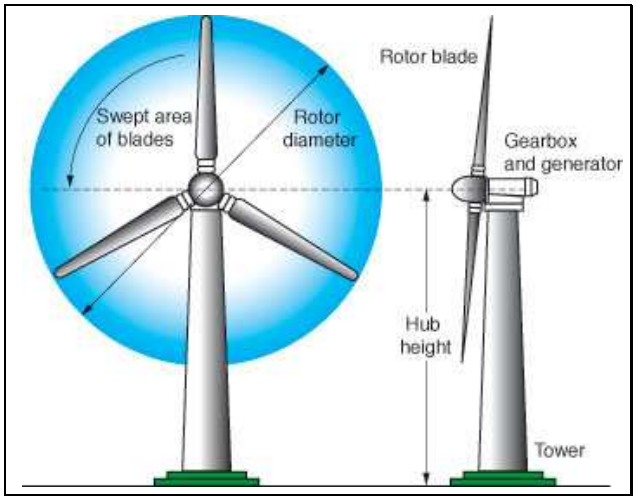

Figure 1.3: A schematic diagram of a modern utility-scale wind turbine (https://str.llnl.gov/AprMay10/mirocha.html).

chapter, relevant information on first-order PBL parameterizations are given with an emphasis on the K-profile approach. Chapter 3 reveals a new physical formulation for the critical bulk Richardson number[2] which was derived from a large-eddy simulation (LES) database. This new formulation resulted in a major amendment to the original (official) YSU scheme. The original and the amended YSU PBL schemes were implemented in an in-house single column model (SCM). In Chapter 4, three idealized LLJ cases (with varying atmospheric stability) were simulated with these schemes. Given the promising results of Chapter 4, the amended YSU PBL scheme was implemented in the WRF model (ver 3.3). In the process of this implementation, a significant computational bug was discovered in the original YSU PBL scheme. This bug was reported to the NCAR and will be fixed in the future release of the WRF model (J. Dudhia, M. Lemone, and S.-Y. Hong, communication by S. Basu). In Chapter 5, the original, the bug-fixed, and the amended versions of the YSU schemes are intercompared for a well-known LLJ case study. Both the bug-fixed and the amended versions performed very well in comparison to the original version. Finally, future directions this work can take are outlined in Chapter 6.

[2]A commonly used statistic for the identification of the boundary layer height; it is a key variable for the YSU PBL scheme.

Chapter 2

Background

In this chapter, brief overviews are provided of (a) planetary boundary layer, (b) low-level jet, and (c) first-order PBL parameterizations with an emphasis on the K-profile approach.

2.1 Planetary Boundary Layer

The planetary boundary layer (PBL) is the lowest part of the atmosphere that is the most affected by the presence of the surface. It is a dynamic layer where the height can be as high as a few kilometers during the daytime and as low as a few hundred meters during the nighttime [Stull, 1988a]. Typically the temporal length of disturbances within the PBL is anywhere from a couple of minutes to a few hours. These disturbances can be anything from swirling motion of air known as eddies, to gust fronts from thunderstorm downdrafts. The dynamic nature of the PBL follows a diurnal pattern driven by surface forces as can be seen in Figure 2.1 [Stull, 1988a]. It is important to note that the PBL structure is more prominent under quiescent synoptic conditions dominated by high surface pressure; this is because low surface pressure tends to 'upset' the PBL by vertically accelerating the surface air [Stull, 1988a].

The convective boundary layer (CBL), or mixed layer, is a class of PBL that occurs during the daytime hours from sunrise to sunset. This part of the PBL is characterized by buoyantly driven turbulence formed when the Sun heats the surface. Once warmed, the surface releases heat upwards in the form of positive sensible heat flux. When these air parcels are heated they become buoyant and rise vertically, creating thermals throughout the depth of the PBL. The vertical velocity of individual thermals could be $O(1)$ m s^{-1} under quiescent conditions. Once these thermals reach the top of the PBL they hit a layer of neutrally/stably stratified air known as the entrainment layer, which is the interface between the PBL and the troposphere, or free atmosphere (FA). This process of impinging thermals on the overlying stable layer can cause gravity waves to develop. Often, when thermals reach this layer the air cools and slowly begins

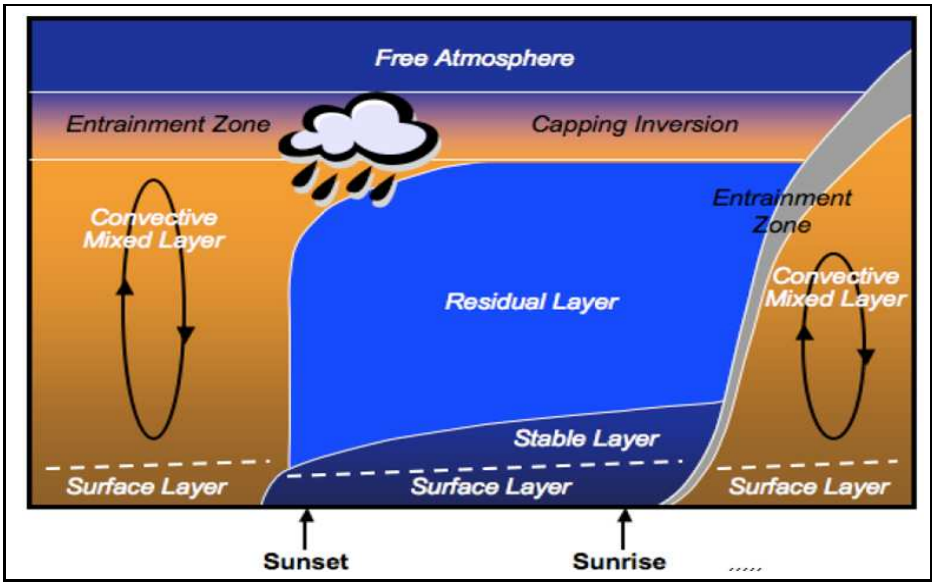

Figure 2.1: Diurnal evolution of the planetary boundary layer. Adapted from Stull [1988a]; image courtesy: Jerome Fast.

to sink. Even though the synoptic-scale upward motion and subsidence are $O(0.1)$ m s^{-1}, they play important roles in the CBL dynamics and should not be neglected. The ascending motion (updrafts), coupled with sinking motion (downdrafts), creates large eddies of the size of the PBL depth. The CBL becomes well mixed and the temperature, water vapor, and wind speed values become nearly uniform throughout the depth of the PBL (with the exception of the near-surface layer).

When the Sun sets, the surface is progressively cooled due to outgoing terrestrial radiation. This process causes the heat flux to become negative and leads to the formation of the stable boundary layer (SBL). Negative heat flux signifies the cooling of the atmosphere because the heat is now being transfered down towards the ground instead of upward. In the SBL, turbulence is generated by wind shear and is destroyed by static stability and molecular viscosity. Due to this competition between shear-generation and buoyancy-destruction, turbulence in the SBL is very weak and the height of the boundary layer is quite shallow (on the order of a few tens to a few hundred meters). Under conditions of strong stratification, the near-surface layer can partially decouple from the atmospheric layer aloft. Under this scenario, flow acceleration of the upper stratified layer can occur leading to the formation of the low-level jets (see the discussion below).

2.2 Low-Level Jets

Low-level jets (LLJs) typically reside at the top or within the nocturnal SBL and develop on almost every continent throughout the globe [Rife et al., 2010]. Currently, there are four major hypotheses describing LLJ development: Inertial Oscillation (IO) [Blackadar, 1957], blockage [Wexler, 1961], sloping terrain [Holton, 1967], and upper-level dynamics [Uccellini and Johnson, 1979].

Inertial Oscillation

The IO concept was first proposed by Blackadar in 1957. His hypothesis was based on the idea that wind speeds aloft fluctuate around the geostrophic wind in a damped oscillatory pattern. These wind speeds are above the geostrophic value (supergeostrophic) during the nighttime and below (subgeostrophic) during the daytime [van de Wiel et al., 2010]. The governing equations for what is known as the Blackadar's model begin with the boundary layer equations for the mean wind components [Blackadar, 1957]:

$$\frac{\partial U}{\partial t} = fV + \frac{\partial \frac{\tau_x}{\rho}}{\partial z} \tag{2.1}$$

$$\frac{\partial V}{\partial t} = f(G - U) + \frac{\partial \frac{\tau_y}{\rho}}{\partial z} \tag{2.2}$$

where τ_x and τ_y values represent the zonal and meridional frictional forces, respectively; f is the Coriolis term [van de Wiel et al., 2010]; U and V illustrate the zonal and meridional wind speed values, respectively; and G represents the zonal geostrophic wind. Please refer to Appendix-A for the full derivation of the Blackadar's model. The resulting solutions are given by Equations (A.9) and (A.10). Figure 2.2 illustrates the IO represented by these equations. What is noticeable is that the wind speed profile does have an oscillating pattern around the geostrophic equilibrium. One can also notice that the wind speed values monotonically decrease from the surface to upper layer; in other words, the wind speed profile does not portray any jet profile. Clearly, this is not observed in the atmosphere and shows a flaw in the Blackadar's hypothesis.

Recently, van de Wiel et al. [2010] expanded the model of Blackadar [1957]. They also utilized Equations (2.1) and (2.2), albeit with the assumption of non-zero friction at sunset [van de Wiel et al., 2010]. Van de Wiel's derivation is also reproduced in Appendix-A; Equations (A.15) and (A.16) are their resulting solutions. The resulting IO from these solutions are also illustrated in Figure 2.2. Unlike the wind speed profile from the Blackadar's model, the wind speed profile from van de Wiel et al. [2010] does portray a LLJ profile. More interestingly, this simple analytical model produces evening wind profiles similar to observations, where sur-

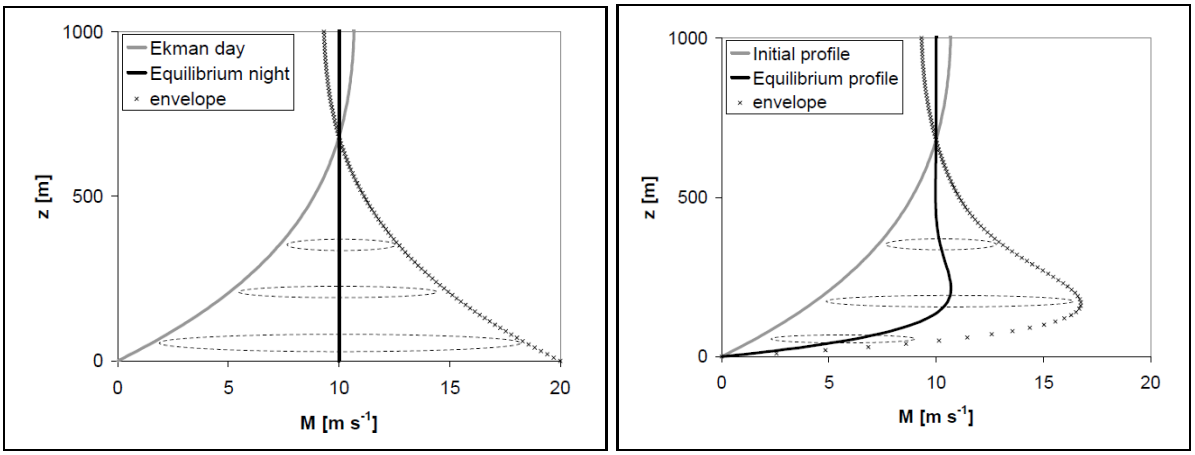

Figure 2.2: Inertial oscillations of the boundary layer wind profiles around equilibrium profiles. The left and right panels represent results from the models by Blackadar [1957] and van de Wiel et al. [2010], respectively. Figure courtesy: van de Wiel et al. [2010].

face wind speeds are at zero increasing to a maximum within the PBL and decreasing again to the equilibrium profile (see van de Wiel et al. [2010] for details).

Instead of solving the boundary layer equations analytically, one can resort to numerical models (e.g., single column or large-eddy model) to study LLJ evolution by IO mechanism. Several articles exist on this topic; see Cuxart et al. [2006] and Beare et al. [2006], and the references therein. In Chapter 4 of this thesis, a single column model will be utilized to simulate IO-generated LLJs.

Blockage

The hypothesis that LLJs form through blockage originated from Wexler in 1961. His hypothesis suggests that LLJs develop through the redirection of air flow due to topography [Wexler, 1961]. An example of this can be seen in the USGP. During the warm season in the United States a phenomenon known as the Bermuda High can come onshore from the Atlantic bringing large scale anti-cyclonic surface flow. With the center of the Bermuda High located somewhere over the southeastern US, the air flow over the central states is southeasterly. As the flow approaches the USGP the air is forced northward by the Rocky Mountains (see Figure 2.3). The accelerated flow to the north over the USGP can assist in the formation of the LLJs in this region.

Sloping Terrain

In 1967, Holton devised another hypothesis for LLJ development associated with gently sloping terrain. Holton describes a reversal of the daytime northerly thermal wind to a nighttime

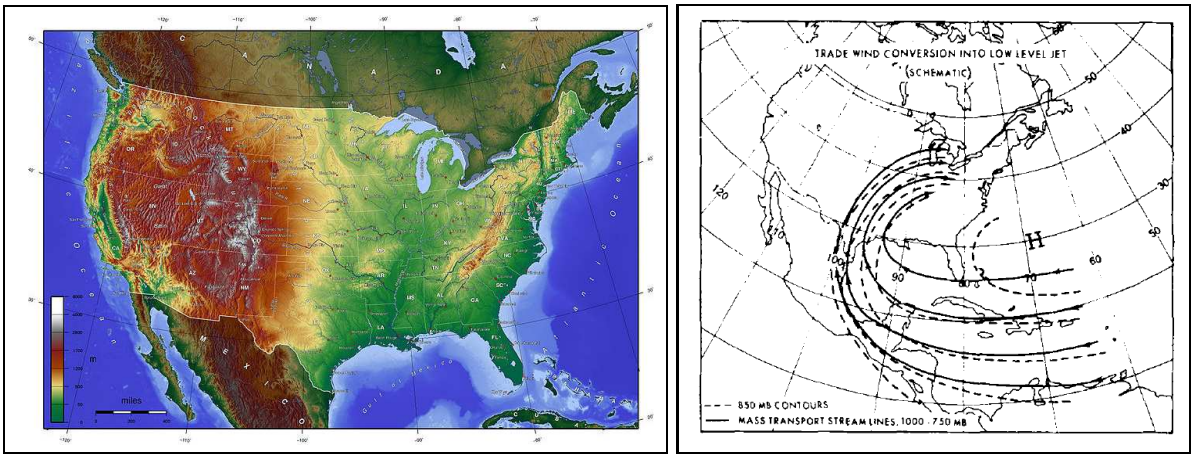

Figure 2.3: Left panel: US topography map (http://en.wikipedia.org/wiki/Geography_of_the_United_States); right panel: Bermuda high coming onshore and associated flow [Wexler, 1961].

southerly thermal wind [Stull, 1988a]. The thermal wind represents the geostrophic vertical shear induced by a horizontal temperature gradient. Again, utilizing the USGP as an example, the terrain increases in height from the east to the west. At a constant pressure/height level the air to the east would be cooler than the terrain in the west. This temperature gradient generates a thermal wind with a northerly shear component. After sunset, the surface cools more rapidly than the overlying air. For this reason, the air just above the surface to the west becomes cooler than the elevated air to the east, creating the opposite affect to occur; thus a southerly shear component is generated. This enhancement of the southerly shear helps the real wind become supergeostrophic during the evening hours. When the wind just above the surface becomes supergeostrophic, a maximum of wind speed, or LLJ, develops. The process of the thermal wind switching directions from daytime to nighttime is detailed in Figure 2.4.

Upper Level Dynamics

The PBL is sometimes sensitive to upper level dynamics; Uccellini and Johnson [1979] describes the connection between synoptic-scale features and mesoscale LLJs (i.e upper-level jet (ULJ) streaks and associated mid-latitude cyclones). When there is a ULJ present, two transverse ageostrophic circulations develop in the entrance and exit regions. In the right entrance region of a ULJ there is divergence aloft and convergence near the surface forming an ageostrophic circulation, this increases the southerly wind component at the surface. If this increase in southerly wind at the surface is amplified a LLJ may develop; this process is illustrated in Figure 2.5.

The southerly flow invoked by these transverse circulations may be further amplified by

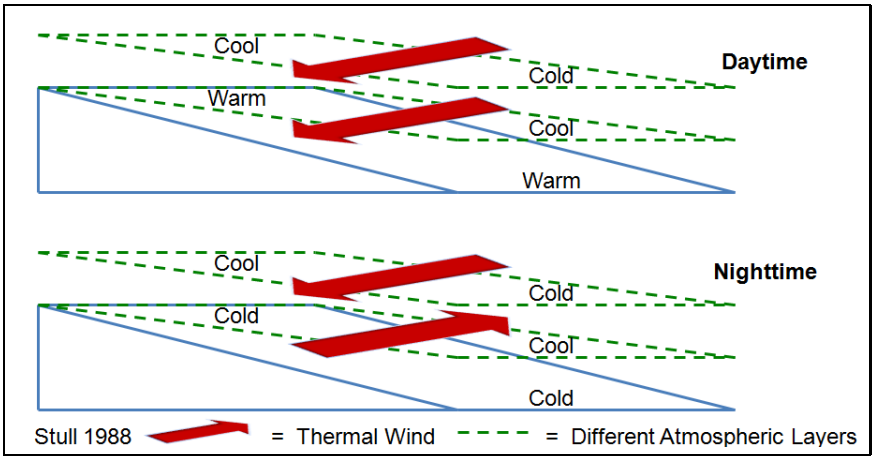

Figure 2.4: A schematic diagram of terrain induced LLJ. This figure is adapted from Stull [1988a].

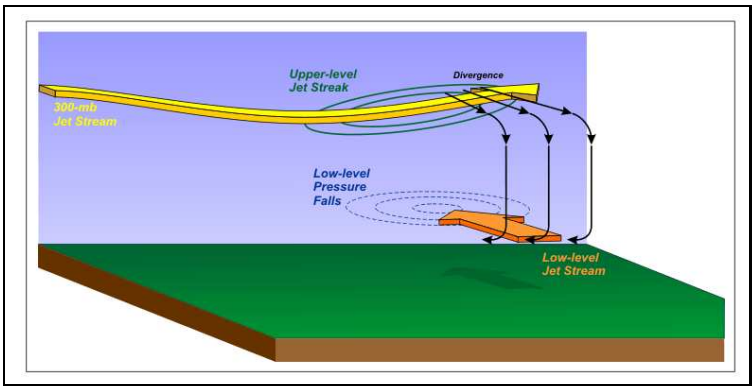

Figure 2.5: Upper-level jet secondary circulations and how they affect LLJs (https://courseware.e-education.psu.edu/courses/meteo361/Section02p02.html).

the diabatic processes associated with synoptic scale cyclones [Uccellini and Johnson, 1979]. As described in the above paragraph, adiabatic processes may independently induce southerly flow due to upper level divergence and subsequent surface convergence in the ULJ exit region; however, when diabatic processes, such as latent heat release, are included then the southerly flow at the surface increases thereby intensifying the LLJ [Uccellini and Johnson, 1979]. The process through which this amplification occurs begins with the southern side of the ULJ warming aloft and cooling at the surface; alternatively, the opposite occurs for the northern side of the ULJ. The processes of latent heat release and condensation in the locations of these warm and cool anomalies then acts to tighten the isentropes thus intensifying the isallobaric wind (shown as black arrow on the right image in Figure 2.6). Overall this circulation is an adjustment toward geostrophic balance that is thermally indirect and entails flow across the jet

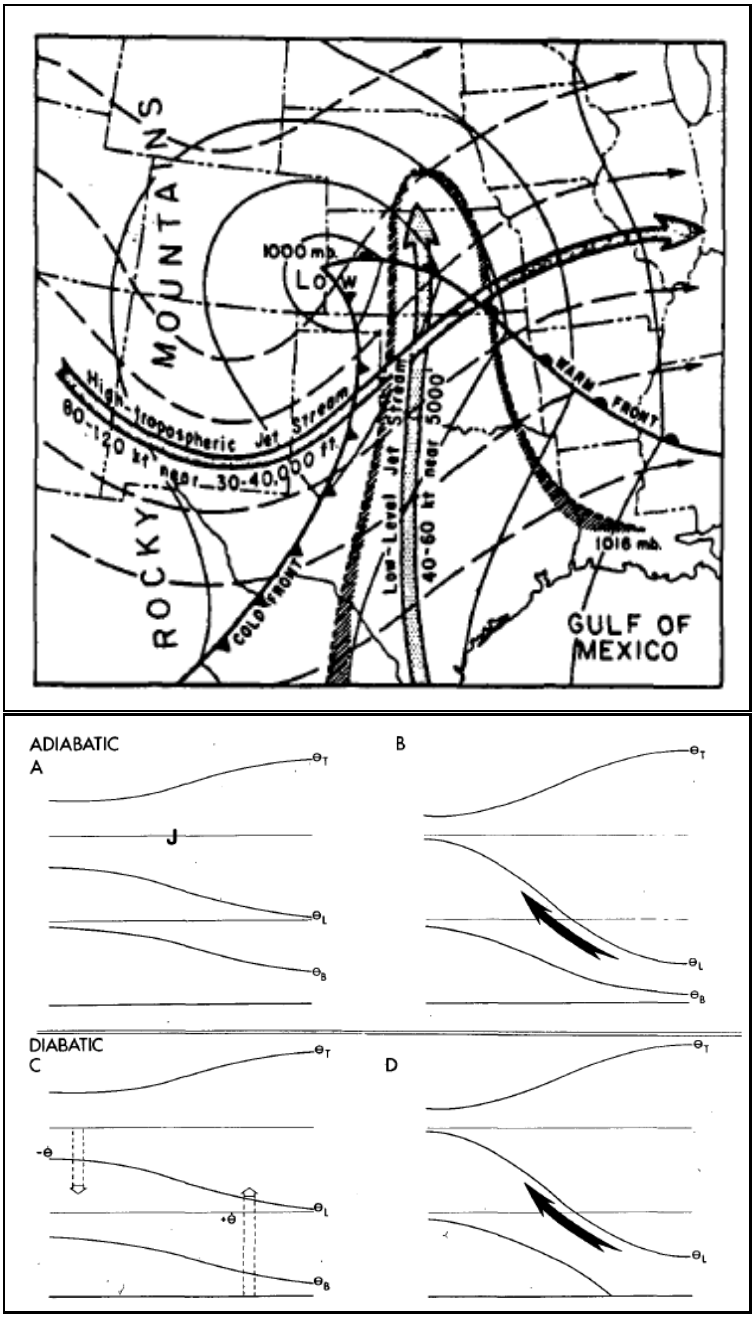

Figure 2.6: Top panel: cyclone; bottom panel: adiabatic and diabatic effects on upper level jet transverse circulations. These figures are adapted from Uccellini and Johnson [1979].

from warm to cold in the low levels. This stronger wind forms as a result of tighter gradients, and helps to develop the PBL LLJ. Figure 2.6 (top) reveals the location of a typical cyclone and associated ULJ; a cross section of this ULJ and associated cyclone illustrates the effect of

diabatic processes on LLJ intensity (Figure 2.6 bottom).

In summary, all the aforementioned mechanisms are important for the formation of LLJs to certain degrees (unfortunately, not quantified in the literature). In this thesis, the focus is on the LLJs which have substantial impacts on the wind energy developments. These specific LLJs have peaks around 100-200 m AGL. In the boundary-layer meteorology community, there is a general consensus that these low-LLJs are predominantly formed by the IO mechanism, which is essentially modulated by the PBL processes. The other three mechanisms rely on outside factors for accelerating the wind (e.g., topography, baroclinity) and are site-specific. For example, over the USGP, the IO-generated LLJs are likely strengthened by the sloping terrain and the blockage mechanisms. However, these two mechanisms cannot explain the omni-present LLJs over the Netherlands (see case study in Chapter 5); these jets are formed primarily by the IO mechanism. The influence of upper layer dynamics on the low-LLJs is possibly negligible. A recent paper by Parish and Oolman [2011] found that the nighttime LLJ maxima are the result of an IO of the unbalanced components that arise fundamentally from frictional decoupling. Diurnal heating of the sloping terrain forces a cycle in the geostrophic wind that is out of phase with the wind maximum.

2.3 First-order PBL Parameterizations

> "The role of a boundary layer scheme in a numerical weather prediction model is to provide the coupling with the surface, to give realistic forecasts of near surface parameters as temperature, specific humidity and wind and to provide input to the cloud and convection schemes" Beljaars and Viterbo [1998].

In an operational NWP model, first-order PBL schemes are commonly used to specify the turbulent flux of a generic quantity ϕ at a given model level proportional to the vertical gradient of that quantity using the concept of eddy-viscosity/diffusivity:

$$\langle w\phi \rangle = -K_\phi \frac{\partial \phi}{\partial z} \tag{2.3}$$

where $\langle w\phi \rangle$ and K_ϕ represent vertical turbulent flux and eddy-diffusivity, respectively. ϕ could be momentum (m), heat (h), moisture (q), or other scalars.

One of the most widely used first-order formulation for the eddy viscosity of momentum (K_m) is the so-called K-profile approach [Troen and Mahrt, 1986, Stensrud, 2007]. O'Brien [1970] was one of the first researchers to propose a K-profile which portrays desirable surface layer behavior, attains a maximum value within the PBL, and decreases to a background diffusion level above the PBL. These behaviors are illustrated in Figure 2.7.

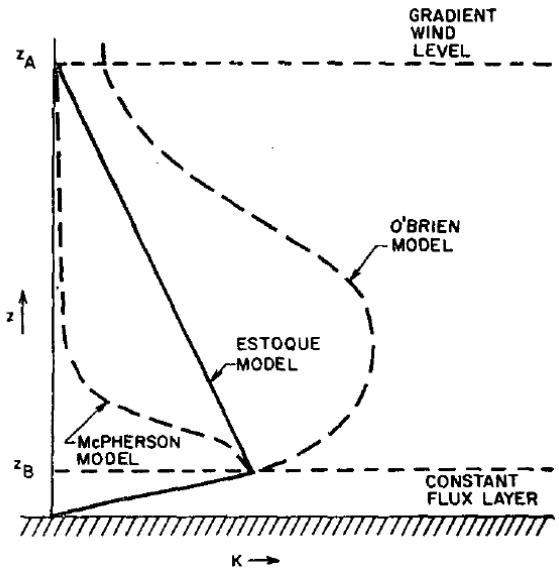

Figure 2.7: A schematic diagram of K profiles in the PBL. This figure is taken from O'Brien [1970]

Based on a second-order closure model-generated database, Brost and Wyngaard [1978] proposed an alternative K-profile formulation suitable for stably stratified conditions:

$$\frac{K_m}{\kappa u_* h} = \frac{\frac{z}{h}\left(1-\frac{z}{h}\right)^p}{1+4.7\left(\frac{z}{h}\right)\left(\frac{h}{L}\right)} \tag{2.4}$$

where $\kappa = 0.4$ and is known as the Von Karman constant; $p = 1.5$; u_* is the surface friction velocity; h is the boundary layer height; and L is known as the Monin-Obukhov length [Stull, 1988a]. Since the YSU PBL scheme utilizes a variant of Equation (2.4), inherent properties of this equation is described in detail here.

Property 1:

For neutrally stratified flows $\frac{z}{L}$ equals to zero. Equation (2.4) reduces to:

$$\frac{K_m}{\kappa u_* h} = \frac{z}{h}\left(1-\frac{z}{h}\right)^p \tag{2.5}$$

For $\frac{z}{h} << 1$ (i.e., in the surface layer), Equation 2.5 further reduces to:

$$K_m = \kappa z u_* \tag{2.6}$$

From Equation (2.6), one can deduce the logarithmic law of the wall. This law solves for the

wind profile within the surface layer to show the effects of the surface friction. This derivation is provided in Appendix-B.

Property 2:

For stably stratified surface-layer flows (i.e., $\frac{z}{L} \neq 0$ and $\frac{z}{h} << 1$), Equation (2.4) simplifies to the well-known surface layer equation by Businger et al. [1971]:

$$K_m = \frac{\kappa u_* z}{1 + 4.7\frac{z}{L}} \tag{2.7}$$

One can derive the stability-corrected logarithmic law of the wall from this equation (not shown here).

Property 3:

Figure 2.8 indicates that as stability increases (larger $\frac{h}{L}$[1]) then the K_m maximum decreases in value and height [Brost and Wyngaard, 1978]. This property is important to note as certain variants of the K-profile approach violates this property (discussed in Chapter 4).

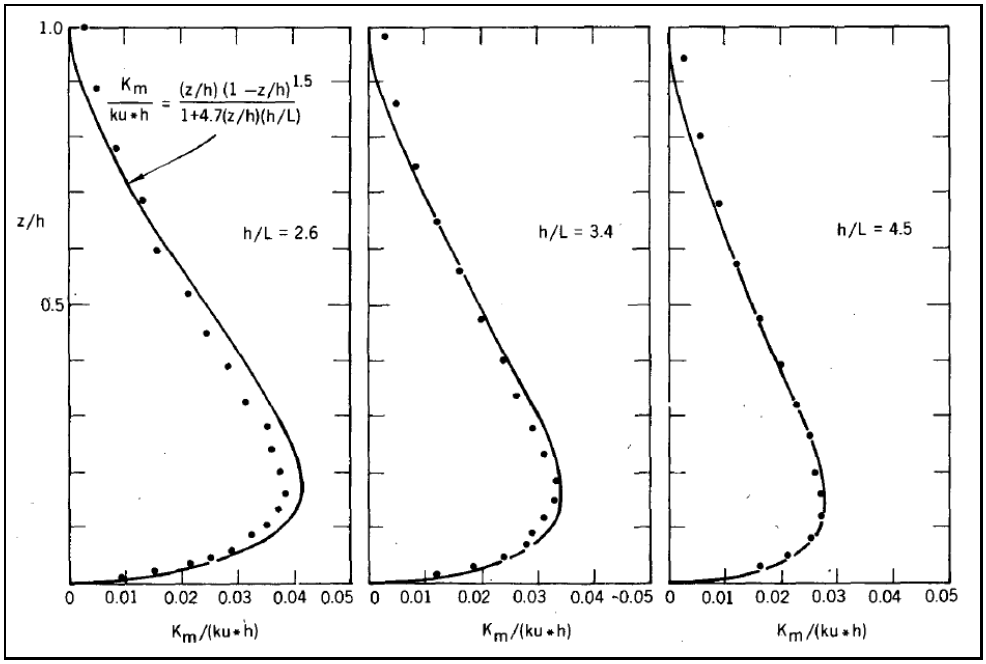

Figure 2.8: K_m profiles for three different stability values. The solid line represents Equation (2.4) and dots represent a second-order closure model generated data. This figure is taken from Brost and Wyngaard [1978].

[1] $\frac{h}{L}$ is a measure of dynamic stability of the entire boundary layer. It goes to zero for neutrally stratified conditions; for very stable flows it reaches high positive values (on the order of 10). For $\frac{h}{L} > 10$, the boundary layer is dominated by intermittent turbulence instead of continuous turbulence.

K_m profiles based on Equation (2.4) are quite dependent on the exponent p. Based on the second-order model-generated database, Brost and Wyngaard [1978] found p to be equal to 1.5. In the absence of reliable field observations Troen and Mahrt [1986] used an integer value of $p = 2$. The local scaling hypothesis by Nieuwstadt [1984] also leads to $p = 2$. On the other hand, based on field experiment data from Minnesota, Sorbjan found $p = 1$ (see Sorbjan [1989]). Based on the analyses of an extensive large-eddy simulation (LES) database, Basu (2012, unpublished work) found p to vary within the range of 1 and 2. Given the uncertainty in the estimation of p from observational and modeled data, in this thesis, p is assumed to be equal to 2, which is also used by most of the contemporary K-profile approaches (including the YSU PBL scheme).

Boundary layer height, h, also impacts the K_m profiles significantly. Typically, critical bulk Richardson number-based parameterizations are used for the estimation of h. In the following chapter, detailed descriptions are provided on this topic.

Chapter 3

Critical Bulk Richardson Number

A major part of this chapter has been submitted as a peer-reviewed article for the Boundary-Layer Meteorology journal.

3.1 Introduction

The critical[1] bulk Richardson number, Ri_{Bc}, is commonly defined as:

$$Ri_{Bc} = \frac{g}{\Theta_{vS}} \frac{\Theta_v(h) - \Theta_{vS}}{U(h)^2 + V(h)^2} h \tag{3.1}$$

where g is the gravitational acceleration; h is the height of atmospheric boundary layer (ABL); $\Theta_v(h)$ is the virtual potential temperature at h; Θ_{vS} is virtual potential temperature near surface; and $U(h)$, $V(h)$ are the horizontal components of velocity at h. For many decades, Ri_{Bc} has been frequently used to determine h in observational [e.g., Hanna, 1969, Heinemann and Rose, 1990, Seibert et al., 1998, Andreas et al., 2000, García et al., 2002] as well as in modeling studies [Troen and Mahrt, 1986, Holtslag et al., 1990, Holtslag and Boville, 1993, Hong, 2010, to name a few]. Over the same period of time, the scientific community has been in active pursuit of the estimation of a 'universal' Ri_{Bc}. For example, Mahrt [1981] analyzed observational data from the Wangara field campaign [Clarke et al., 1971] and found that the frequency distribution of Ri_{Bc} has a mean of $\sim$ 0.55 and mode of $\sim$ 0.3. More recently, Vogelezang and Holtslag [1996] utilized a multi-year observational dataset from a 200 m tall meteorological tower and a collocated sodar in Cabauw, the Netherlands, to better estimate Ri_{Bc}. For stably stratified conditions, they demonstrated that if one slightly modifies the conventional definition of Ri_{Bc} [i.e., Eq. (3.1)] by excluding the frictional effects of the near-

[1] In the 1970s, this particualr Richardson number was referred to as boundary layer bulk Richardson number. Currently, the boundary-layer meteorology community refers to it as 'critical' bulk Richardson number. We believe that the usage of the word 'critical' is inappropriate.

surface layer, one can significantly improve the reliability of its estimation. Their estimated values of (modified) Ri_{Bc} ranged from ~ 0.2 to ~ 0.3. The same year, Sørensen et al. [1996] tried to estimate the optimal Ri_{Bc} based on approximately one hundred radio soundings from Copenhagen, Denmark. They calculated the root-mean-square relative error of h as a function of Ri_{Bc} and revealed the results in Figure 3.1. They found that the error is minimized to $\sim 30\%$ when Ri_{Bc} is around 0.14. Zilitinkevich and Baklanov [2002] summarized these aforementioned studies along with many other endeavors to estimate Ri_{Bc} in their Table II (Table 3.1). Perusing this table, it is quite obvious that Ri_{Bc} is not a universal constant; it can range from $O(0.1)$ to $O(1)$ for ABL data. Nonetheless, the quest for the 'holy grail' of a universal Ri_{Bc} continues in the twenty-first century [e.g., Jeričević and Grisogono, 2006, Esau and Zilitinkevich, 2010].

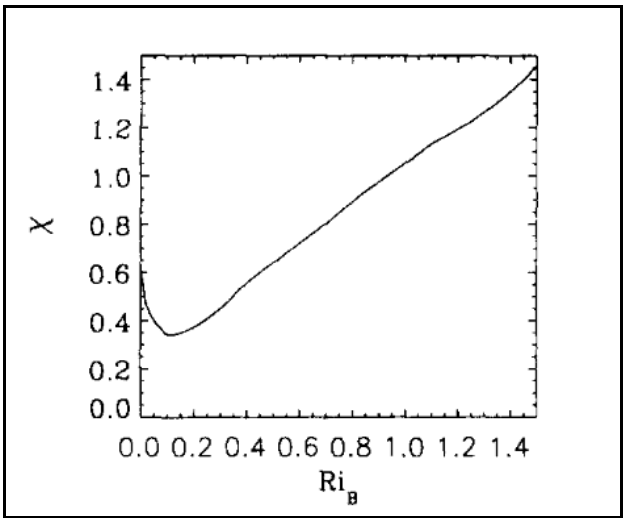

Figure 3.1: Root-mean-square relative error of the ABL heights as a function of the critical value of the bulk Richardson number. Radiosonde are utilized. This figure is taken from Sørensen et al. [1996].

Table 3.1: Zilitinkevich and Baklanov [2002] Table 2

Reference	$\mathbf{z}_1, m$	z_2, m	$Ri_{\{B,F\}c}$	**Comments**
Laikhtman (1961)	0	0	1.65	Ri_B in terms of geostrophic wind, data from Main Geophysical Observatory expeditions in Russia

Table 3.1 – continued

Hanna (1969)	0	0	0.33-0.56	Ri_B in terms of temperature gradients in the lowest 100m, data from O'Neill Nebraska
Melgarejo and Deardorff(1974)	0	0	Average 0.55 typical 0.3	
Brost and Wyngaard (1978)	1	1	0.11-0.22	Data from measurements and second-order closure model
Anisimova et al. (1978)	0	0	up to 7	Lab experiments with downslope drainage flows (analyzed by Mahrt, 1982)
Zeman (1979)	$\frac{1}{2}h$	$\frac{1}{2}h$	0.5	Data on nocturnal jets over the Great Plains, O'Neill; h compared with the Brost-Wyngaard closure model
Mahrt et al. (1979)	2	0	average 0.3-0.5 maximum 15	Data from Wangara, Risø, O'Neill and Haswell; h compared with h_u
Mahrt (1981)	0	0	0.5-1.0	Typical values of Ri_{Bc} or Ri_{Fc} from different sources
	2			
Wetzel (1982)	2	0	0.33	Wangara data (mainly for the radiation dominated SBL) with different estimates of h
Troen and Mahrt (1986)	0	0	0.5	Data from LES (Deardorff model) and Wangara experiment
Byzova et al. (1989)	0	0	0.6-1.0	Data on turbulence and mean profiles from 300-m tower, Obninsk, Russia, 1972-1974
Heineman and Rose (1990)	2	0	0.3-0.55 typical 0.33	Tethered balloon sounding, Filchner/Ronne Ice Shelf, Antarctica; h compared with h_u, the Zilitinkevich (1972) SBL height scale, and the height, h_o, of the lowest θ gradient discontinuity
Holtslag et al. (1990)	2	0	0.25-0.5	Best fit for radiosounding data from de Bilt
Holtslag and Boville (1993)	10	0	0.5	Modelling and radiosonde data from several sites

Table 3.1 – continued

Sorensen et al. (1996)	30	0	0.14-0.24	Ri_b from either HIRLAM or radiosoundings, h from radiosoundings at weakly stable SBL, jaegersborg
Vogelezang and Holtslag (1996)	20	20	(i) 0.21-0.22	(i) For the nocturnal SBL
	40	40	(ii) 0.30-0.32	(ii) for well-mixed SBL both from Cabauw mast data and SODAR data (for h)
	80	80		
Fay et al. (1997)	0	0	0.38	Ri_B from German NWP model and actual h from either radiosoundings or second-order closure model
Makshtas et al. (1998)	2	0	0.4	Ri_F from aerological and balloon observations over the Weddell Sea; h compared wit wind-maximum and inversion heights (h_u and h_i)
Andreas et al. (2000)	0	0	0.4	Ri_B from radiosoundings at the Ice Station Weddell; h compared with h_u and h_i

So far, only a handful of studies attempted to probe the relationships of Ri_{Bc} with other physical variables. One of the notable studies is the one by Zilitinkevich and Baklanov [2002] who reported (weak) functional dependencies of Ri_{Bc} with composite variables involving free flow stability, the Coriolis parameter, etc. Furthermore, they speculated that Ri_{Bc} might also be dependent on the aerodynamic surface roughness ($z_\circ$). In line with this speculation, Gryning and Batchvarova [2003] reported very low value of Ri_{Bc} (specifically, 0.03) for marine ABL (i.e., low $z_\circ$ in contrast to typical land surface). In a comprehensive study, Vickers and Mahrt [2004] analyzed stable boundary layer (SBL) data from two field sites over land (Kansas and Colorado, the USA) and a location over ocean (near Atlantic seaboard of the USA). Even though the scatter in Figure 3.2 from Vickers and Mahrt [2004] is substantial, a trend of decreasing Ri_{Bc} with decreasing $z_\circ$ is discernible. For each case represented the surface roughness values decreased from CASES99 over Kansas (largest $z_\circ$) to CBLAST over the ocean (lowest $z_\circ$). Their results provided further observational support for the speculation by Zilitinkevich and Baklanov [2002].

In this paper, we use an extensive large-eddy simulation (LES) database to characterize Ri_{Bc} in barotropic stable boundary layers. We find that Ri_{Bc} is strongly dependent on h/L, where L is the surface Obukhov length [Stull, 1988b, Garratt, 1992]. The dependence of Ri_{Bc}

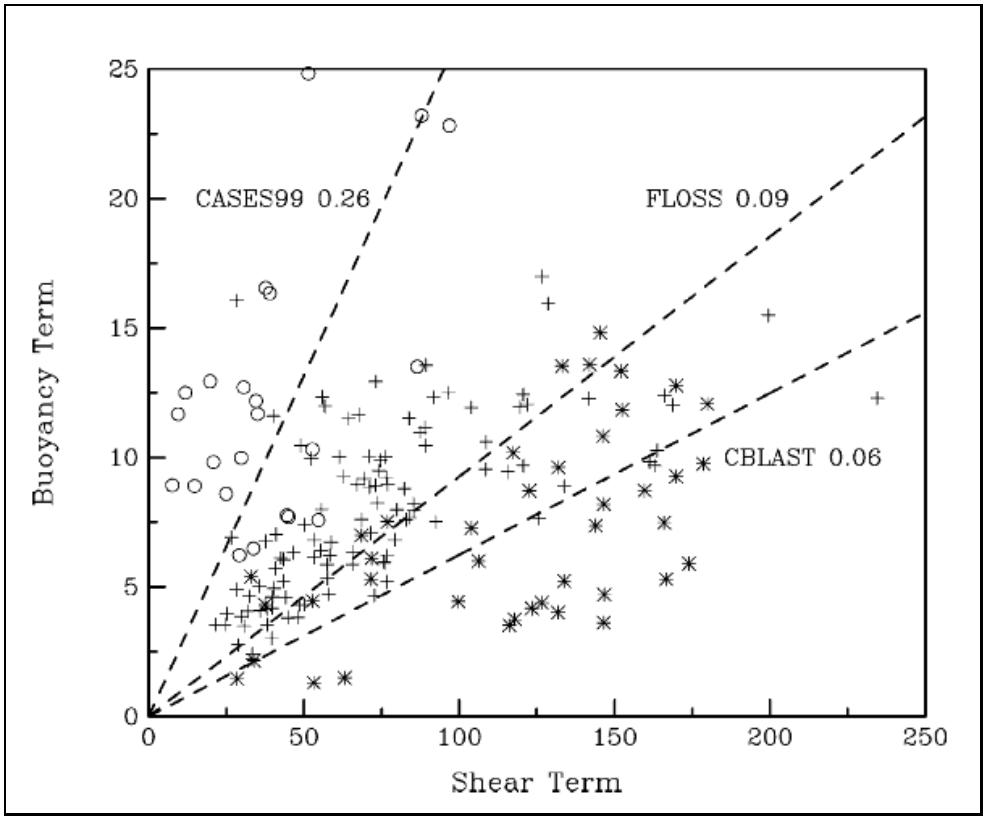

Figure 3.2: Buoyancy term versus shear term calculated from three field campaigns. Dashed lines show the least square fits forced through the origin. Printed values are the slope, equivalent to the critical bulk Richardson number. This figure is taken from Vickers and Mahrt [2004].

on $z_\circ$ is found to be weaker. To our surprise, qualitatively similar dependencies were reported forty years ago by Melgarejo and Deardorff [1974], based on the well-known resistance laws[2]. To the best of our knowledge, these dependencies have been forgotten by the boundary layer community.

The organization of this chapter is as follows. In Section 3.2, we describe the LES database. Various characteristics of the simulated Ri_{Bc} are discussed in Section 3.3. In Section 3.4, we provide an algorithm along with examples to estimate h using h/L-dependent Ri_{Bc}. We envisage that this simple algorithm can be effectively used in observational and modeling studies in lieu of the constant Ri_{Bc}. We emphasize the limitations of our current study in Section 3.5 and provide some final remarks.

[2]Resistance laws are well-known similarity relationships involving wind velocity at the upper boundary of the ABL, its thickness, air temperature difference between the upper and the lower boundaries of the ABL, roughness of the underlying surface, and buoyancy forces.

3.2 Description of Large-Eddy Simulation Database

3.2.1 LES Code

In this study, an in-house large-eddy simulation code (called MATLES) is utilized for the creation of a high-resolution, four-dimensional SBL turbulence database. The salient features of the MATLES code are as follows: (i) the code solves the filtered incompressible Navier-Stokes equations written in rotational form; (ii) derivatives in the horizontal directions are computed using the Fourier Collocation method, while vertical derivatives are approximated with second-order central differences; (iii) dealiasing of the non-linear terms in Fourier space is done using the 3/2 rule; (iv) explicit second-order Adams-Bashforth time advancement scheme is used; (v) spectral cutoff filtering is used in the horizontal directions (no explicit filtering is performed in the vertical direction); (vi) only Coriolis terms involving horizontal wind are considered; and (vii) a staggered vertical grid is used. A tuning-free (dynamic) SGS model, called the locally-averaged scale-dependent dynamic (LASDD) model was used for all the simulations.

The potential of the LASDD SGS model was established in simulations of stably stratified boundary layers [Basu and Porté-Agel, 2006, Basu et al., 2006], neutrally buoyant boundary layers [Anderson et al., 2007], observed diurnal cycle [Basu et al., 2008b], and radioactive scalar dispersion [Vinuesa et al., 2007]. Overall, the agreements between the LES-generated turbulence statistics and some well-established empirical formulations (e.g., the local scaling hypothesis) as well as theoretical predictions (e.g., Kolmogorov spectra) were remarkable. Most importantly, the LASDD SGS model performed quite well in the surface layer (in terms of proper near-wall SGS dissipation behavior). We would like to mention that the MATLES code was recently utilized to setup the control case for the GEWEX Atmospheric Boundary Layer Study (GABLS) 3^{rd} LES Intercomparison project [Basu et al., 2011].

3.2.2 Initial, Boundary, and Forcing Conditions

In the LES-ABL approach, idealized or observed soundings (i.e., 1-D vertical profiles) of velocity and other atmospheric variables (such as potential temperature) in conjunction with small-scale random perturbations (noise) are typically used to generate initialization fields. With the help of the filtered Navier-Stokes equations, and similar prognostic equations for scalar variables (e.g., potential temperature), these fields are then evolved in time under the constraints of certain large-scale forcing terms (e.g., geostrophic wind) and boundary conditions (e.g., prescribed surface temperature). Usually, it takes about an hour of simulation (depending on the characteristics of the boundary layer to be simulated) to generate realistic turbulence (i.e., to develop the inertial range of the spectra).

In this study, the following equations are used to generate the initial profiles:

$$U(z) = G - D_G \quad \text{for} \quad z_\circ < z \leq H_i \tag{3.2a}$$

$$U(z) = G \quad \text{for} \quad z > H_i \tag{3.2b}$$

$$V(z) = 0 \quad \text{for} \quad z_\circ < z \tag{3.2c}$$

$$W(z) = 0 \quad \text{for} \quad z_\circ < z \tag{3.2d}$$

$$\Theta(z) = 300 \quad \text{for} \quad z_\circ < z \leq H_i \tag{3.2e}$$

$$\Theta(z) = 300 + N\,(z - H_i) \quad \text{for} \quad z > H_i \tag{3.2f}$$

where U, V, and W are the longitudinal, lateral, and vertical velocity components, respectively. G and D signify geostrophic wind speed and geostrophic departure, respectively. Θ denotes potential temperature. N is the so-called inversion strength. The variables z, $z_\circ$, and H_i denote height above surface, aerodynamic roughness length, and initial boundary layer height, respectively. Random Gaussian noise with standard deviations of 0.1 ms^{-1} and 0.1 K are added to the lowest 100 m of the vertical velocity and potential temperature fields, respectively.

Time-height independent geostrophic wind speed (signifying barotropic SBL) is used as a forcing term for all the LES runs. In the past, numerous SBL modeling studies have used sensible heat flux as a lower boundary condition [Brown et al., 1994, Saiki et al., 2000, Jiménez and Cuxart, 2005, to name a few]. In Basu et al. [2008a], the fundamental shortcomings of such sensible heat flux-based lower boundary conditions were discussed. Based on analytical and numerical results, it was shown that if the surface sensible heat flux is prescribed as a boundary condition, only the near-neutral to weakly stable regime will be captured; in order to represent the moderate to very stable regime in a simulation, surface temperature prescription or prediction is required. Holtslag et al. [2007] provides further insights into this topic. For these reasons, we use surface temperature as a lower boundary condition. For every LES run, the surface cooling rate (C) is kept at a constant value.

In this study, 82 different combinations of individually varying G, D_G, C, $z_\circ$, H_i, N, and f are considered. The ranges of these initial, boundary, and forcing conditions are given in Table 3.2.

Table 3.2: Ranges of the Initial, Boundary, and Forcing Conditions

G (m s^{-1})	D_G (m s^{-1})	C (K h^{-1})	$z_\circ$ (m)	H_i (m)	N (K km^{-1})	f (s^{-1})
6–18	0–8	0.5–2	0.01–0.1	50–300	3–100	8×10^{-5}–12×10^{-5}

3.2.3 Numerical Details

The selected domain size for all the LES-ABL runs is 800 m × 800 m × 790 m. This domain is divided into 80 × 80 × 80 (i.e., grid resolution of 10 m × 10 m × 10 m). The time step is equal to 0.1 s and is kept the same for all the runs. Each run is of 12 h (i.e., 432,000 time steps) in duration. Hourly-averaged data from the last 6 h of each simulation is used in this paper for calculating Ri_{Bc} and other variables. In total, we have $6 \times 82 = 492$ samples for all the analyses.

3.2.4 Comparison With DATABASE64

We would like to note that our database is qualitatively quite similar to the LES-ABL database (called DATABASE64) created by Esau and his co-workers [e.g., Esau and Zilitinkevich, 2006]. In our view, the major difference is that the DATABASE64 uses sensible heat flux-based surface boundary condition, which is inappropriate for SBL simulations [Basu et al., 2008b]. We consider the other differences in terms of LES subgrid-scale model, spatial resolution, etc., to be minor.

3.3 Results

Following Mahrt [1981] and numerous other studies, we assume h equals the height of the simulated low-level jet core. From the 492 hourly-averaged profiles, we then extract h, $U(h)$, $V(h)$, and $\Theta(h)$. Since our LES runs do not include specific humidity, we use potential temperature instead of virtual potential temperature. Since the lowest model level is at 5 m, Θ_S denotes potential temperature at that height.

In Figure 3.3 (left panel), we plot the buoyancy term $\left(\frac{g}{\Theta_S}\left(\Theta(h) - \Theta_{vS}\right)h\right)$ against the shear term $\left(U(h)^2 + V(h)^2\right)$. The scatter in Figure 3.3 is quite large ($r^2 = 0.69$) and qualitatively similar to Figure 4 of Vogelezang and Holtslag [1996] and Figure 5 of Vickers and Mahrt [2004]. In order to better understand the distribution of the 492 samples, we partition them in three stability classes: $0 < h/L \leq 5$ (336 samples, filled-circle symbols), $5 < h/L \leq 10$ (140 samples, star symbols), and $h/L > 10$ (16 samples, square symbols). The relative magnitude of shear and buoyancy terms for these classes are quite different, as would be physically expected.

The best-fit linear regression line (with the constraint of passing through the origin) in Figure 3.3 (left panel) represents $Ri_{Bc} = 0.15$. Vogelezang and Holtslag [1996] performed a similar analysis of the observational data from the Cabauw tower and reported $Ri_{Bc} = 0.22$. In comparison, Vickers and Mahrt [2004] found $Ri_{Bc} = 0.26, 0.09, 0.06$ from the CASES99, FLOSS, and CBLAST datasets, respectively. They attributed this variation in Ri_{Bc} to roughness length differences among the field sites.

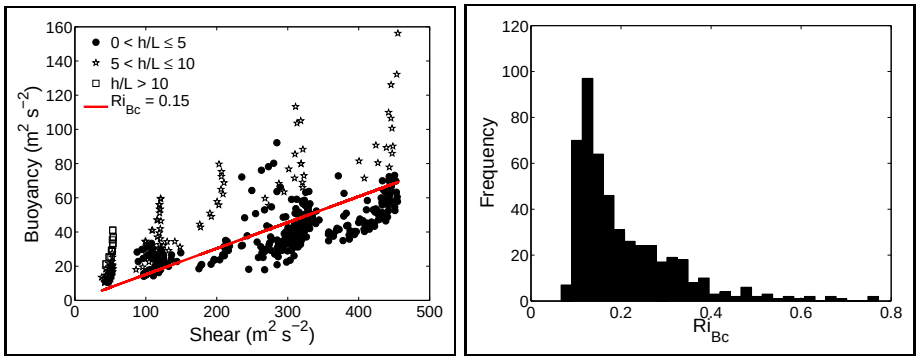

Figure 3.3: Left panel: the numerator (buoyancy) and denominator (shear) of Eq. (3.1) are plotted against each other. The filled-circle, square, and star symbols represent three stability classes: $0 < h/L \leq 5$, $5 < h/L \leq 10$, and $h/L > 10$, respectively. The red line denotes the best-fit linear regression line (with the constraint of passing through the origin). The slope of this line is $Ri_{Bc} = 0.15$. Right panel: the frequency histogram of Ri_{Bc}.

From each of the 492 shear-buoyancy pairs, one can calculate corresponding Ri_{Bc} value. The frequency historgram of this Ri_{Bc} is shown in Figure 3.3 (right panel). The mean, median, and mode of the distribution are: 0.21, 0.16, and 0.13, respectively. The distribution is skewed towards high Ri_{Bc} values which are associated with high h/L values (discussed below). We would like to emphasize that the shape of this distribution is entirely dependent on the type of LES runs performed and does not reflect any sort of 'real' ABL climatology. If our LES database had more very stable ($h/L > 10$) runs, the Ri_{Bc} distribution would have been skewed further.

In Figure 3.4 (top-left panel), we plot Ri_{Bc} as a function of h/L. The strong collapse of the data on a straight line (with a slope of 0.045) was surprising and we first suspected spurious self-correlation, since h appears in both Ri_{Bc} and h/L. Therefore, we decided to plot Ri_{Bc}/h versus $1/L$ (Figure 3.4; top-right panel). The slope of the line remains almost unchanged. Therefore, we rule out self-correlation and propose a 'new' relationship:

$$Ri_{Bc} = \alpha \frac{h}{L} \tag{3.3}$$

where α is equal to 0.045. We would like to stress that observational data from various field campaigns are needed to (dis)-prove the validity of this estimate of α.

It was quite difficult for us to believe that the scientific community had never discovered such a simple functional relationship. Thus, we decided to dig further in the literature. We found that the well-cited second-order closure modeling paper by Brost and Wyngaard [1978] did report variation of Ri_{Bc} from 0.11 to 0.22 with increasing stability. Seemingly, they were

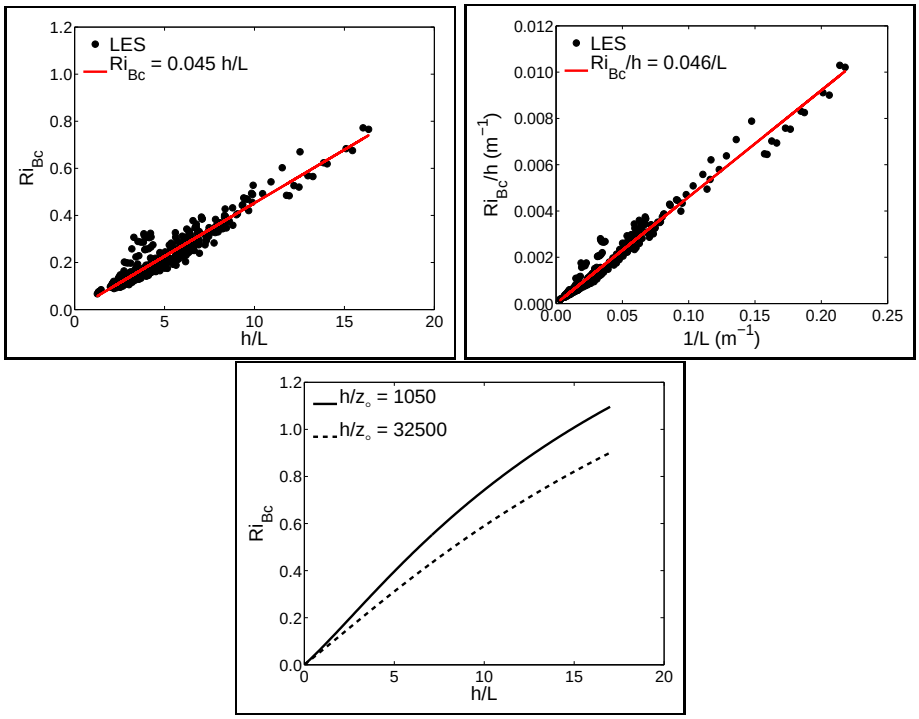

Figure 3.4: Top-left panel: variation of Ri_{Bc} with respect to h/L based on LES-generated samples. The red line denotes the best-fit linear regression line (with the constraint of passing through the origin). Top-right panel: variation of Ri_{Bc}/h with respect to $1/L$ based on LES-generated samples. The red line denotes the best-fit linear regression line (with the constraint of passing through the origin). Bottom panel: variation of Ri_{Bc} with respect to h/L based on Eq. (3.4). The solid and dashed lines represent $h/z_\circ = 1050$ and 32500, respectively.

looking for a constant Ri_{Bc} and did not probe into the stability-dependency of Ri_{Bc} any further. However, an older paper by Melgarejo and Deardorff [1974] did propose a relationship between Ri_{Bc} and h/L (utilizing the well-known resistance laws):

$$Ri_{Bc} = \frac{1}{Pr}\frac{h}{L}\frac{\log\left(\frac{h}{z_\circ}\right) - C}{\left[\log\left(\frac{h}{z_\circ}\right) - A\right]^2 + B^2} \tag{3.4}$$

where A, B, and C are the so-called similarity functions; and Pr is Prandtl number. Based on the observations from the Wangara field campaign Clarke et al. [1971], Yamada [1976] proposed the following similarity functions (valid for the range of h/L considered in this paper):

$$A = 1.855 - 0.380\frac{h}{L} \tag{3.5a}$$

$$B = 3.020 + 0.300\frac{h}{L} \tag{3.5b}$$

$$C = 3.655 - 0.829\frac{h}{L} \tag{3.5c}$$

In Figure 3.4 (bottom panel), we plot Eq. 3.4 utilizing Eq. 3.5. Following Yamada [1976], we assume $Pr = 0.74$. In our LES database, the maximum and minimum values of $h/z_\circ$ are 1050 and 32500, respectively. These numbers are used in Figure 3.4 (bottom panel) to provide upper and lower bounds of the Ri_{Bc} vs. h/L curves, respectively. By comparing the top-left and the lower panels of Figure 3.4, we claim that qualitatively the LES-derived results are quite similar to Eq. 3.4. The Ri_{Bc} values predicted by Eq. 3.4 are a bit higher. This could be due to the fact that the definition of Θ_S is different in Eq. 3.4. Melgarejo and Deardorff [1974] considered Θ_S to be the potential temperature at $z_\circ$. From Figure 3.4, it is also clear that for the ranges of h/L considered in this paper, the importance of surface roughness is low. We explore this issue further using Figure 3.5.

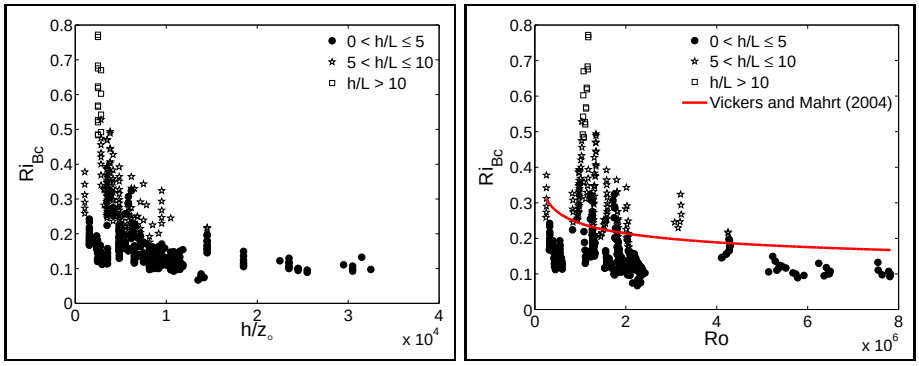

Figure 3.5: Lef panel: Ri_{Bc} as a function of $h/z_\circ$. Right panel: Ri_{Bc} as a function of surface Rossby number (Ro). The red line represents Eq. 3.6. In both the panels, the filled-circle, square, and star symbols represent three stability classes: $0 < h/L \leq 5$, $5 < h/L \leq 10$, and $h/L > 10$, respectively.

In Figure 3.5, we plot Ri_{Bc} as functions of $h/z_\circ$ and surface Rossby number ($Ro = \frac{M_{10}}{f z_\circ}$). To facilitate direct comparison with the results reported by Vickers and Mahrt [2004], we use 10 m wind speed, M_{10}, in the definition of the surface Rossby number. On the right panel of Figure 3.5, we have also overlayed the following relationship between Ri_{Bc} and Ro proposed by Vickers and Mahrt [2004]:

$$Ri_{Bc} = 0.16\left(10^{-7}Ro\right)^{-0.18} \tag{3.6}$$

When we consider the aggregated dataset (i.e., all the 492 samples), we see a decreasing trend of Ri_{Bc} with increasing $h/z_\circ$ or Ro in (see Figure 3.5). Figure 6 of Vickers and Mahrt [2004] reported a qualitatively similar trend and in turn proposed Eq. 3.6. However, when we consider individual stability classes (see different symbols in Figure 3.5), the relationship becomes very weak. This information might explain the large scatter of Ri_{Bc} reported by Vickers and Mahrt [2004] in the case of CASES99 (land site) dataset and not in the CBLAST (marine site) dataset. Over land, one would expect large variation of h/L but not so much over marine locations. Thus, we speculate that the large values of Ri_{Bc} (as high as 0.5) reported by Vickers and Mahrt [2004] were not due to high roughness, but rather due to high stability. At this point, we are unable to provide conclusive evidence on this topic.

3.4 Practical Applications

Following Troen and Mahrt [1986], h is traditionally determined from an observed or a modeled sounding in an iterative manner using a constant Ri_{Bc} [e.g., the Weather Research and Forecasting – WRF model's YSU scheme assumes $Ri_{Bc} = 0.25$ over land; Hong, 2010]. Holtslag et al. [1990] described this iterative process succinctly (we modified the notations to be consistent with the present work): "The computation starts with calculating the bulk Richardson number (Ri_B) between the level of Θ_S and subsequent higher levels of the model. Once Ri_B exceeds the critical value (Ri_{Bc}), h is derived with linear interpolation between the level with $Ri_B > Ri_{Bc}$, and the level underneath."

Based on our findings, we believe that the assumption of constant Ri_{Bc} is quite inappropriate for modeling studies. According to Eq. 3.3, by setting Ri_{Bc} as a constant, one implicitly constrains the bulk stability of the modeled boundary layers. Thus, we propose to replace constant Ri_{Bc} with stability-dependent Ri_{Bc}, which does not suffer from such inappropriate constraint. The only change to the existing algorithm will be: at every model level, the value of Ri_{Bc} will be computed (instead of prescribed) based on the current height and surface Obukhov length. This revised algorithm is described below:

Algorithm 3.4.1: H_ESTIMATION(z, L, U, V, Θ)

comment: Given Obukhov length (L) and vertical profiles of U, V, and Θ

comment: Estimate h

comment: z^k denotes height of the sounding or model levels (k)

$\alpha = 0.045$
$\Theta_S \leftarrow \Theta\left(z^{k=1}\right)$

for $k \leftarrow 2$ **to** k_{max}

do
$$\begin{cases} Ri_B^k \leftarrow \frac{g}{\Theta_S} \frac{\Theta\left(z^k\right) - \Theta_S}{\left[U\left(z^k\right)\right]^2 + \left[V\left(z^k\right)\right]^2} z^k \\ Ri_{Bc}^k \leftarrow \alpha \frac{z^k}{L} \\ \textbf{if } Ri_B^k \geq Ri_{Bc}^k \\ \quad \textbf{then} \begin{cases} \Delta R_+ = Ri_{Bc}^k - Ri_B^k \\ \Delta R_- = Ri_{Bc}^{k-1} - Ri_B^{k-1} \\ h \leftarrow \frac{\Delta R_+ z^{k-1} - \Delta R_- z^k}{\Delta R_+ - \Delta R_-} \\ BREAK \end{cases} \end{cases}$$

In Figure 3.6, we provide two examples illustrating the strength of the proposed algorithm. The left panels show two simulated low-level jets. The simulation shown on the top-panel used geostrophic wind of 12 m s^{-1}, whereas the bottom one used relatively low geostrophic wind of 6 m s^{-1}. Since other initial, boundary, and forcing conditions of both the simulations were exactly the same, the bottom-panel simulation ($h = 75$ m) represents more strongly stratified condition in comparison to the top-panel run ($h = 155$ m). In the right panels, Ri_B and Ri_{Bc} are plotted as function of height. Clearly, the cross-over points (top: $Ri_{Bc} = 0.40$; bottom: $Ri_{Bc} = 0.70$) are collocated with the respective low-level jet peaks (i.e., h). In other words, the stability-dependent Ri_{Bc} can capture the boundary layer height with high accuracy.

3.5 Concluding Remarks

The major finding of this study is that the critical bulk Richardson number (Ri_{Bc}) is not a constant, rather it strongly depends on the stability parameter (h/L). Its dependency on surface roughness is found to be weaker. Even though similar results were reported by Melgarejo and

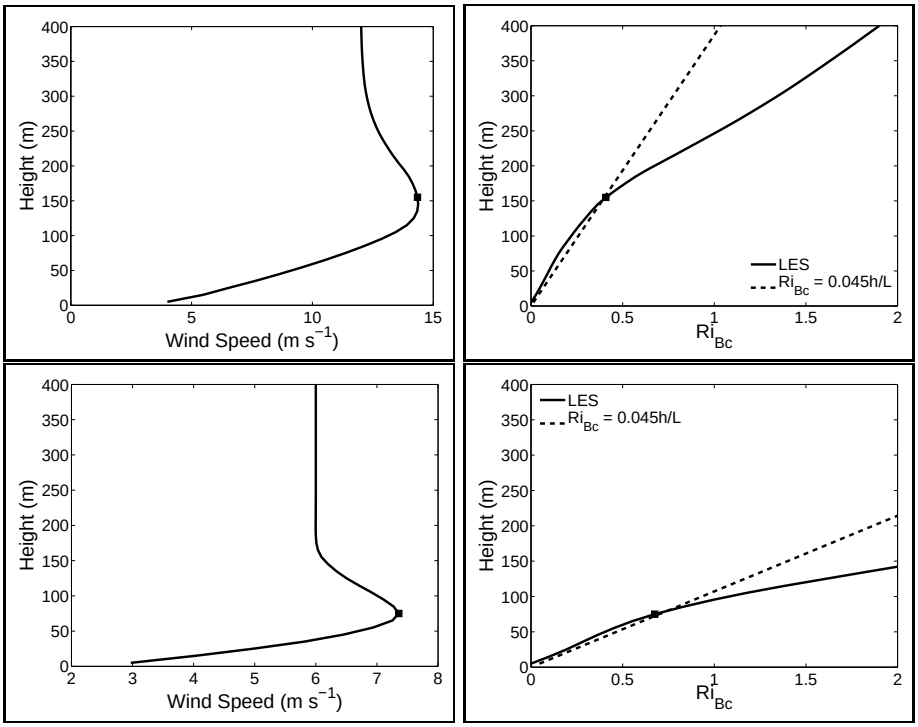

Figure 3.6: Left panels: simulated low-level jets using $G = 12$ m s^{-1} (top) and $G = 6$ m s^{-1} (bottom).Right panels: profiles of simulated Ri_B and estimated Ri_{Bc}. See text for details.

Deardorff [1974] about forty years ago, surprisingly they never received any serious attention from the scientific community. Instead, the community at large remained engaged on the futile attempt to estimate a universal Ri_{Bc}. In a way, we have reinvented the wheel. However, we strongly believe that this 'reinvention' was necessary to improve the estimation of h in various practical applications (e.g., dispersion modeling).

Even though our results are based on an extensive LES database, we were unable to cover the entire parameter space. For example, we only focused on stably stratified flows. The roughness values we considered are representative of typical land surfaces rather than water bodies. We are performing more LES runs which will eventually fill these voids in our LES database. In the near future, we also anticipate increasing the spatial resolution in the flow fields to ~ 5 m. We acknowledge that our LES database currently contains only idealized runs, which are not representative of 'real-world' SBL turbulence. This is due to the fact that these simulations do not include (i) the effects of natural topography and land-surface heterogeneities; (ii) baroclinicity, large-scale advection, and subsidence effects; and (iii) interactions among several physical processes—e.g., turbulence, radiative transfer, and cloud microphysics. We are currently developing a coupled mesoscale-LES modeling framework which will enable us to

perform more realistic LES runs.

Last, given the significance of the LES-based results reported in this paper, their validation utilizing observational data is urgently needed. We encourage our colleagues with access to high-quality observational data to confront this challenge.

Chapter 4

Single Column Modeling

4.1 Introduction

Since the contemporary PBL schemes in NWP and climate models are mostly one-dimensional, it is quite common to test these schemes in offline modes prior to implementing in operational models. The stand-alone codes which are used to investigate the strengths and weaknesses of the PBL schemes are known as the single column models (SCMs). For example, before the official release of the YSU, ACM2, and QNSE PBL schemes they were tested in single column models (see Hong et al. [2006], Pleim [2007a], Sukoriansky et al. [2005]).

It is also a common practice to test different PBL schemes by intercomparing several single column model output and by validating against observations and/or large-eddy simulation results. For example, during the first GEWEX[1] Atmospheric Boundary Layer Study (GABLS) SCM intercomparison study Cuxart et al. [2006], eleven models were compared against the LES-generated results (Figure 4.1). These results helped show that the operational PBL schemes develop diffuse LLJs and in turn overestimates LLJ heights and underestimates LLJ wind speeds. In contrast, the research schemes can somewhat produce results close to the LES values; however, the diversity among various PBL schemes-generated results was large.

In this chapter, the strategy of the aforementioned first GABLS SCM intercomparison study is followed. Different versions of the YSU scheme (discussed later) are incorporated in the NCSU-SCM code. Using this code, three idealized LLJ cases of varying stability are simulated and compared against the LES-generated output.

[1] Global Energy and Water Cycle Experiment

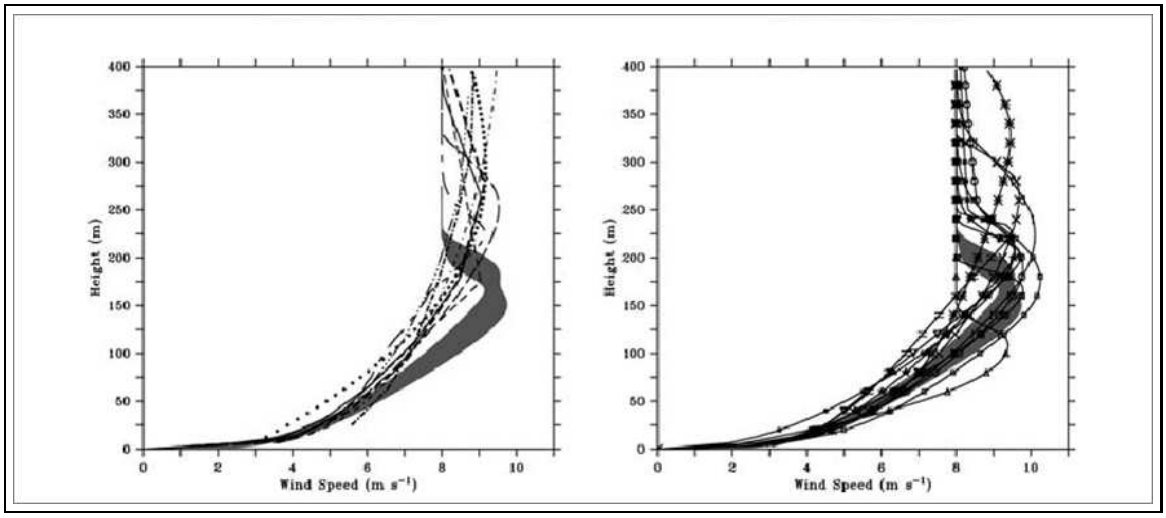

Figure 4.1: Low-level jets simulated by operational (left panel) and research (right panel) PBL schemes. An ensemble of LES-generated profiles are plotted as a gray band for comparison. This figure is taken from Cuxart et al. [2006].

4.2 Description of SCM Code

The salient features of the SCM code (called the North Carolina State University NCSU-SCM code) used in this chapter are as follows: (i) it solves the governing equations for the atmospheric boundary layer with the assumptions of incompressibility and horizontal homogeneity (Eqs. 4.1); (ii) vertical derivatives are approximated with second-order central differences; (iii) the explicit second-order Adams-Bashforth time advancement scheme is employed; and (iv) a staggered vertical grid is used.

$$\frac{\partial U}{\partial t} = f(V - V_G) - \frac{\partial \langle uw \rangle}{\partial z} \tag{4.1a}$$

$$\frac{\partial V}{\partial t} = -f(U - U_G) - \frac{\partial \langle vw \rangle}{\partial z} \tag{4.1b}$$

$$\frac{\partial \Theta}{\partial t} = -\frac{\partial \langle w\theta \rangle}{\partial z} \tag{4.1c}$$

where U, V, and Θ denote mean longitudinal velocity, lateral velocity, and potential temperature, respectively. The geostrophic wind components are represented by U_G and V_G. f is the Coriolis parameter. The turbulent fluxes are parameterized using local gradient hypothesis as

follows:

$$\langle uw \rangle = -K_m \frac{\partial U}{\partial z} \tag{4.2a}$$

$$\langle vw \rangle = -K_m \frac{\partial V}{\partial z} \tag{4.2b}$$

$$\langle w\theta \rangle = -K_h \frac{\partial \Theta}{\partial z} \tag{4.2c}$$

The eddy viscosity, K_m, is calculated by,

$$K_m = \frac{\kappa z u_*}{\phi_m} \left(1 - \frac{z}{h}\right)^p \tag{4.3}$$

where κ is the von-Karman constant (0.4), z is height above ground, h is the boundary layer height, u_* is the surface friction velocity, and p is a constant. The non-dimensional velocity gradient, ϕ_m, is defined as: $\phi_m = 1 + 5\frac{z}{L}$; where L is the Monin-Obukhov length.

The surface layer parameterization follows Monin-Obukhov similarity theory. For stably stratified conditions, the friction velocity, u_*, is calculated from the mean horizontal wind speed, $M(z_1)$, at the first vertical model level ($z = z_1$) as follows:

$$u_* = \frac{\kappa M(z_1)}{\ln(\frac{z_1}{z_\circ}) + 5\frac{z_1}{L} - 5\frac{z_\circ}{L}} \tag{4.4a}$$

In a similar manner, the surface heat flux is computed as:

$$\langle w\theta \rangle_s = \frac{u_* \kappa \left[\Theta_s - \Theta(z_1)\right]}{\ln(\frac{z_1}{z_\circ}) + 5\frac{z_1}{L} - 5\frac{z_\circ}{L}} \tag{4.4b}$$

where Θ_s and $\Theta(z_1)$ denote the surface temperature and the mean potential temperature at the first model level, respectively. $z_\circ$ is the so-called aerodynamic roughness length.

4.3 YSU PBL Scheme and Its Variants

Table 4.1: YSU PBL Scheme and Its Variants

Scheme	ϕ_m Formulation	Ri_{Bc} Formulation	Reference
YSU_0	$\phi_m = 1 + 5\frac{z_1}{L}$	0.25 (over land)	WRF (ver 3.2 to 3.4)
YSU_1	$\phi_m = 1 + 5\frac{z}{L}$	0.25 (over land)	Brost and Wyngaard [1978]
YSU_2	$\phi_m = 1 + 5\frac{z}{L}$	$Ri_{Bc} = \alpha\frac{h}{L}$	Present thesis
HP96	$\phi_m = 1 + 5\frac{0.1h}{L}$	0.25 (over land)	Hong and Pan [1996], Stensrud [2007]

Equation (4.3) was originally proposed by Brost and Wyngaard [1978]. The properties of this equation were discussed in detail in Chapter 2. One of the key characteristics of this equation is that it allows the peak of the K_m profile to decrease in value and height with increasing stability (see Figure kmfig:5 in Chapter 2). The root of this height dependency of the K_m-peak lies is in the term ϕ_m. If one replaces z in ϕ_m with any fixed term (e.g., $0.1h$), the K_m-peak height becomes independent of stability, which is physically unrealistic. Some of the variants of Equation (4.3) make this inappropriate assumption (see Table 4.1).

From the year 2010 onwards, the WRF model's YSU implementation uses $\phi_m = 1 + 5\frac{z_1}{L}$. In this thesis, this variant is called YSU_0. Since this implementation does not physically make sense, it was believed that the usage of z_1 instead of z is a computational bug. Where z_1 is defined as the first model level. Once this bug was found those who worked on the YSU scheme were contacted (J. Dudhia, M. Lemone, and S.-Y. Hong, personal communication by S. Basu). The bug was acknowledged and a corrected version will be released in the future. This corrected version is called YSU_1 in this chapter.

In another variant, z in ϕ_m is replaced by $0.1h$. This approach has been used by many researchers in the past (see Hong and Pan [1996], Hong et al. [2006], Stensrud [2007]). This implementation is also problematic as it does not allow the height dependency of the K_m-peak. This implementation is called HP96 in this chapter.

YSU_0, YSU_1, and HP96 uses $Ri_{Bc} = 0.25$. In Chapter 3, the fundamental limitation of this approach was discussed and a new relationship was proposed: $Ri_{Bc} = \alpha h/L$. α is a constant, h is the boundary layer height and L is the Monin-Obukhov stability. This new relationship is implemented into the NCSU-SCM code and is called YSU_2. Utilizing an extensive LES database α was found to be 0.045. However, it is anticipated that the value of α in different codes will be dependent on the underlying numerics. However, we speculate that α is not going to be case dependent. In other words, in operational settings (e.g., the WRF-ARW by NCAR), α will remain constant once it is tuned. When comparing several of the NCSU-SCM simulations with the corresponding LES runs, $\alpha = 0.060$ is found to be the optimum and is utilized in all the SCM runs.

4.4 Description of Case Studies

In this chapter, three case studies (with varying stability) are simulated using the NCSU-SCM code. Each case is run with all the four aforementioned schemes (i.e., YSU_0, YSU_1, YSU_2, and HP96) and the results are compared with LES output (see Table 4.2). The SCM and LES runs utilized 80 grid points in the vertical direction (domain height = 790 m, vertical resolution = 10 m). In order to understand the sensitivity of the results with respect to grid resolution, a set of simulations with 20 grid points (vertical resolution = 40m) were run (representative of a

typical mesoscale model setting).
The following geostrophic wind values are used:
Case Study #1: G = 12 m s^{-1}
Case Study #2: G = 9 m s^{-1}
Case Study #3: G = 6 m s^{-1}
For each case the surface cooling rate is kept constant at 0.75 Kh^{-1}; aerodynamic surface roughness ($z_\circ$) is taken equal to 0.03 m, and the Coriolis parameter (f) is assumed to be equal to 10^{-4} s^{-1}. The initial profiles used are similar to the ones reported in Chapter 3. The initial boundary layer height, H_i, is taken equal to 200 m. The imposed capping inversion strength is 3 K per 1000 m.

$$U(z) = G \quad \text{for} \quad z_\circ < z \tag{4.5a}$$
$$V(z) = 0 \quad \text{for} \quad z_\circ < z \tag{4.5b}$$
$$W(z) = 0 \quad \text{for} \quad z_\circ < z \tag{4.5c}$$
$$\Theta(z) = 300 \quad \text{for} \quad z_\circ < z \leq H_i \tag{4.5d}$$
$$\Theta(z) = 300 + N\,(z - H_i) \quad \text{for} \quad z > H_i \tag{4.5e}$$

4.5 Results

When the geostrophic wind is decreased in value the shear generated turbulence is also decreased leading to shallower and more stable boundary layer (Figures 4.2-4.4). Based on Table 4.2 and Figure 4.2, the estimated $\frac{h}{L}$ values for the LES runs are approximately 1.9 for Case Study #1, 4.8 for Case Study #2, and 12.7 for Case Study #3. The wind direction values are reported in Figure 4.3. The magnitude of directional shear measured between the LLJ peak height and the surface is ~ 40. Similar values were reported earlier by Beare et al. [2006] and Basu and Porté-Agel [2006]. Figure 4.4 shows the results for the potential temperature profiles. The LES profiles for Case Studies #1 and #2 reveal convex shapes signifying turbulent SBLs. Nieuwstadt predicted similar results and which were discussed in Basu and Porté-Agel [2006].

Upon closer inspection of the results, YSU_0 scheme performs the worst. YSU_0 creates excessive diffusion smearing out the near surface shear. This scheme creates very high LLJs with excessive cooling (unusually high surface sensible heat flux – see Table 4.2). Similar behavior was reported for mesoscale simulations [Storm and Basu, 2010, Shin and Hong, 2011].

The HP96 model does not perform as poorly as the $YSU_\circ$ but still produces enhanced mixing. Interestingly, HP96 produces similar surface sensible heat flux values as LES but generates more diffusion within the outer SBL layer. For this reason, the SBL is warmer in the

lower layers and cooler in the higher layers.

The largest improvement is found in the YSU_1 run after the bug fix is added (fix acknowledged by the NCAR). However, with increasing $\frac{h}{L}$ YSU_1 creates a negative bias in the LLJ height. This is because the increase in $\frac{h}{L}$ requires a higher Ri_{Bc} value than the set 0.25. With h proportional to Ri_{bc}, YSU_1 has to underestimate LLJ height. This can be seen by viewing Case Study #1 results where Ri_{Bc} is approximately 0.25 so both YSU_1 and YSU_2 are similar. This can be seen in the weakly to moderately stable cases where the value of $\frac{h}{L}$ is around 5 causing the new Ri_{Bc} value to approximately equal 0.25 (same as the constant). This low contrast in Ri_{Bc} values causes both YSU_1 and YSU_2 to perform similarly. In comparison with YSU_1, YSU_2 marginally improved the simulations for wind speed values. The potential temperature profiles from YSU_2 show improvement to a similar caliber as the wind speeds.

The effect of grid resolution is not found to be significant. A coarser resolution creates more diffusion and smoothes out the LLJ peak. Similar behavior was reported by Cuxart et al. [2006] and Beare et al. [2006].

4.6 Conclusions

In the past, mesoscale modeling studies [Storm and Basu, 2010, Shin and Hong, 2011] revealed that the YSU PBL scheme produced enhanced mixing and in turn underestimated LLJ magnitude and overestimating height. The exact cause of this problem had not been identified. In this thesis, the two major contributions involve finding the inappropriate use of the ϕ_m equation and identifying a new formulation $Ri_{Bc} = \alpha\frac{h}{L}$. These contributions lead to two different PBL schemes (called YSU_1 and YSU_2) which show superior performance in simulating idealized low-level jets. However, it is important to note that the major benefit of utilizing this new Ri_{Bc} relationship is not fully illustrated with the presented cases. In the following chapter, these two schemes in addition to the original YSU scheme (YSU_0), will be used and inter-compared for a realistic case utilizing the WRF (version 3.3) model.

Table 4.2: Surface layer characteristics of the simulated SBLs

Case Study #	Grid Points	PBL Scheme/LES	u_* (ms^{-1})	$\langle w'\theta' \rangle$ (K ms^{-1})	L (m)
1	80	LES	0.28	-0.033	52.49
1	80	HP96	0.27	-0.033	44.90
1	80	YSU_0	0.42	-0.070	81.82
1	80	YSU_1	0.29	-0.030	60.91
1	80	YSU_2	0.29	-0.030	61.32
1	20	YSU_1	0.28	-0.032	54.03
1	20	YSU_2	0.29	-0.032	58.24
2	80	LES	0.22	-0.025	31.24
2	80	HP96	0.21	-0.024	27.85
2	80	YSU_0	0.30	-0.042	46.31
2	80	YSU_1	0.21	-0.019	33.87
2	80	YSU_2	0.21	-0.020	32.56
2	20	YSU_1	0.21	-0.023	30.56
2	20	YSU_2	0.21	-0.021	30.64
3	80	LES	0.15	-0.016	15.18
3	80	HP96	0.14	-0.014	13.64
3	80	YSU_0	0.17	-0.019	18.33
3	80	YSU_1	0.12	-0.010	13.67
3	80	YSU_2	0.13	-0.011	13.06
3	20	YSU_1	0.12	-0.011	11.79
3	20	YSU_2	0.12	-0.011	11.06

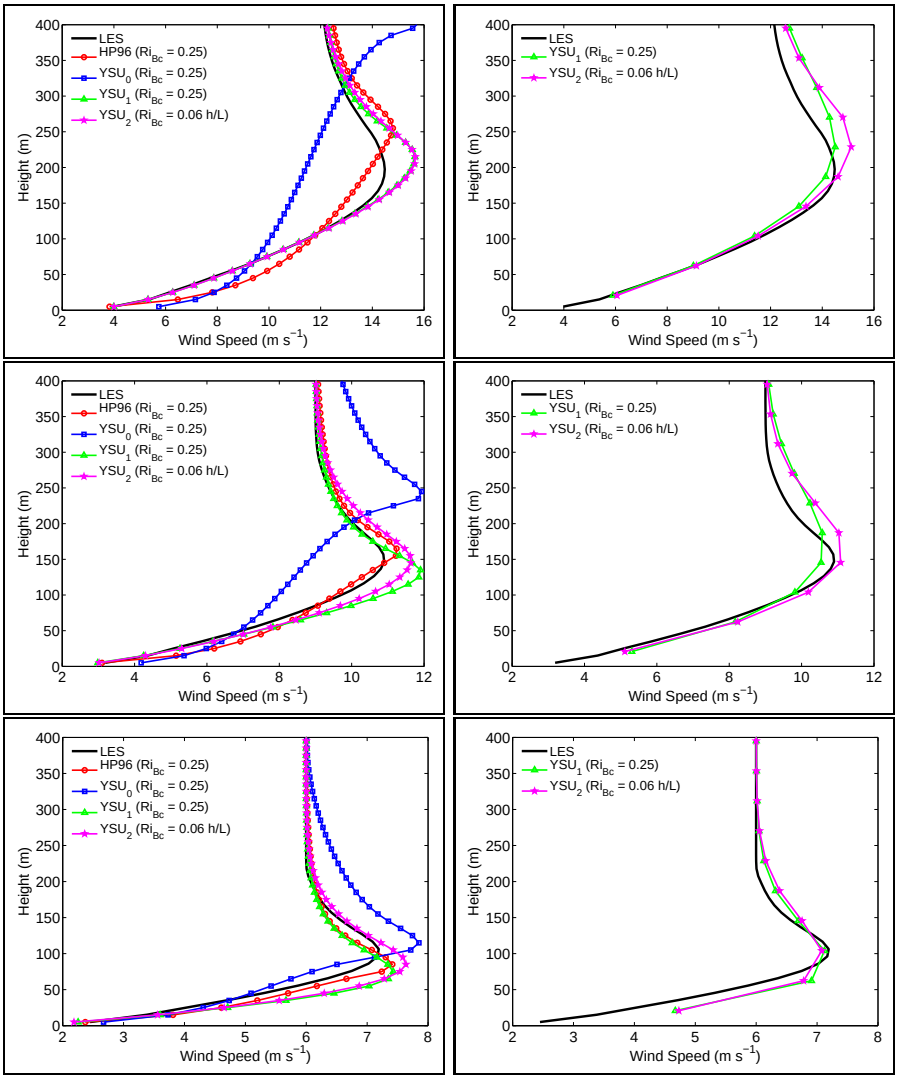

Figure 4.2: The SCM-generated wind speed profiles for Case 1 (top-panel), Case 2 (middle-panel) and Case 3 (bottom-panel). The left and right panels show simulations using 80 and 20 vertical grid points, respectively. The LES-generated profiles (solid black line) are shown for comparison.

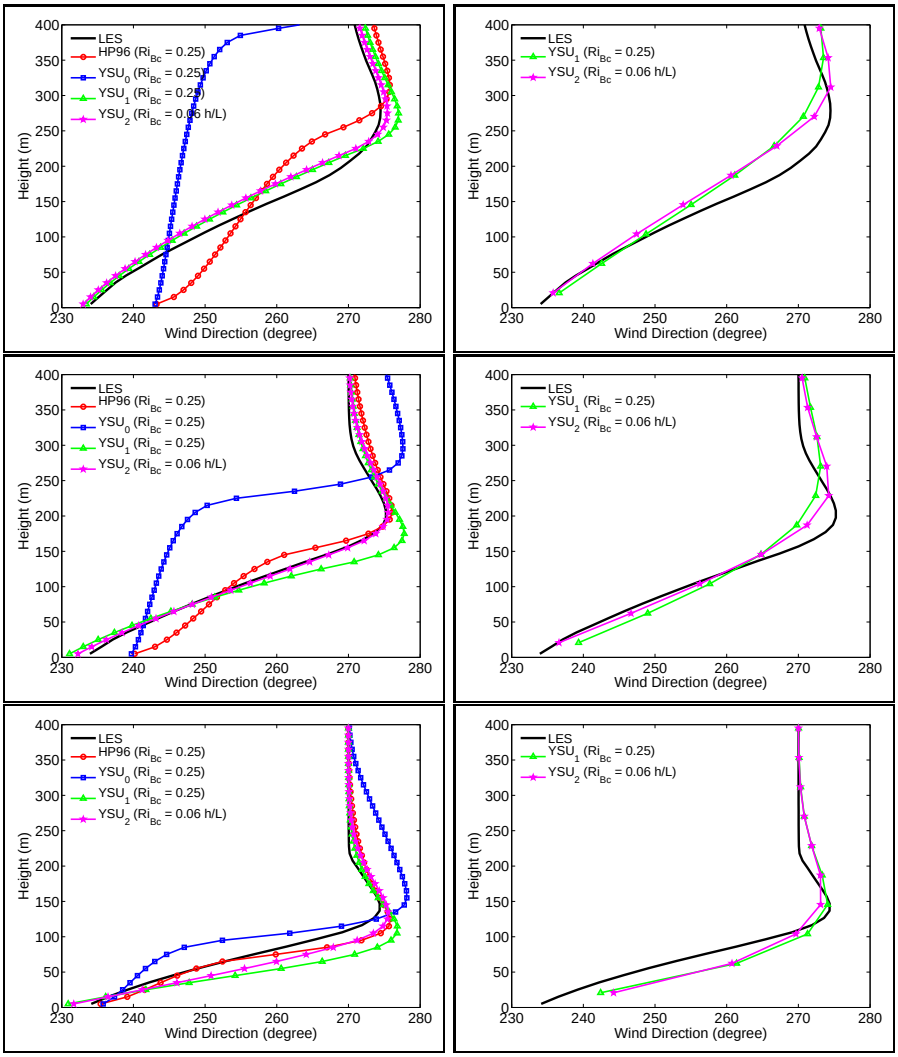

Figure 4.3: The SCM-generated wind direction profiles for Case 1 (top-panel), Case 2 (middle-panel) and Case 3 (bottom-panel). The left and right panels show simulations using 80 and 20 vertical grid points, respectively. The LES-generated profiles (solid black line) are shown for comparison.

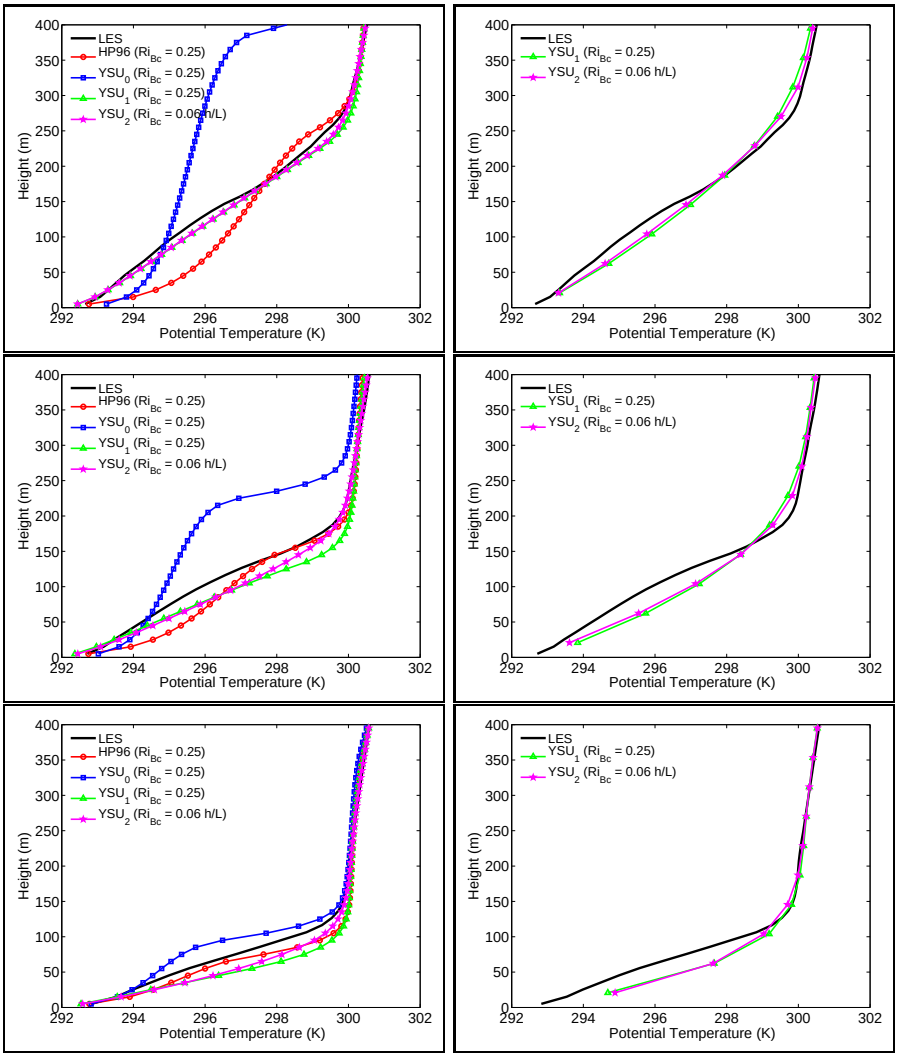

Figure 4.4: The SCM-generated potential temperature profiles for Case 1 (top-panel), Case 2 (middle-panel) and Case 3 (bottom-panel). The left and right panels show simulations using 80 and 20 vertical grid points, respectively. The LES-generated profiles (solid black line) are shown for comparison.

Chapter 5

Mesoscale Modeling

5.1 Introduction

Mesoscale modeling has become very important in modern-day weather forecasting. There are several different parts to a mesoscale model that can affect output and accuracy. One area that greatly effects the accuracy of mesoscale model output are the planetary boundary layer (PBL) schemes. These schemes are associated with some of the greatest sources of uncertainty within mesoscale models [Pleim, 2007b, Shin and Hong, 2011].

In the previous chapter of this thesis, SCM studies were completed utilizing the NCSU-SCM code. The results from these idealized runs revealed that the original Yonsei University (YSU) PBL scheme YSU_0 were improved after a bug fix and implementation of a new equation. The bug fix scheme was referred to as YSU_1 and the scheme with the new equation was referred to as YSU_2. Given that the idealized simulations revealed realistic improvements the next natural step would be to implement these YSU modifications in a mesoscale model. This task is accomplished in the present chapter. The YSU_1 and YSU_2 schemes are implemented in the Weather Research and Forecasting (WRF) model (ver 3.3). The performance of the different variants of the YSU PBL scheme is tested by simulating the third GEWEX Atmospheric Boundary Layer Study (GABLS) case study. The simulation results are then validated against observations.

5.2 Description of Case Study

GABLS is an ongoing collaborative study formed to better understand the stable boundary layer physics (see Bosveld et al. [2012] and the references therein). Recently, the third modeling intercomparison study (called GABLS3 case) was released under the auspices of GABLS. This case study involves a 9 hour time period on July 2nd, 2006 00UTC to 09UTC. The location of interest is Cabauw, The Netherlands where the Cabauw experimental site for atmospheric

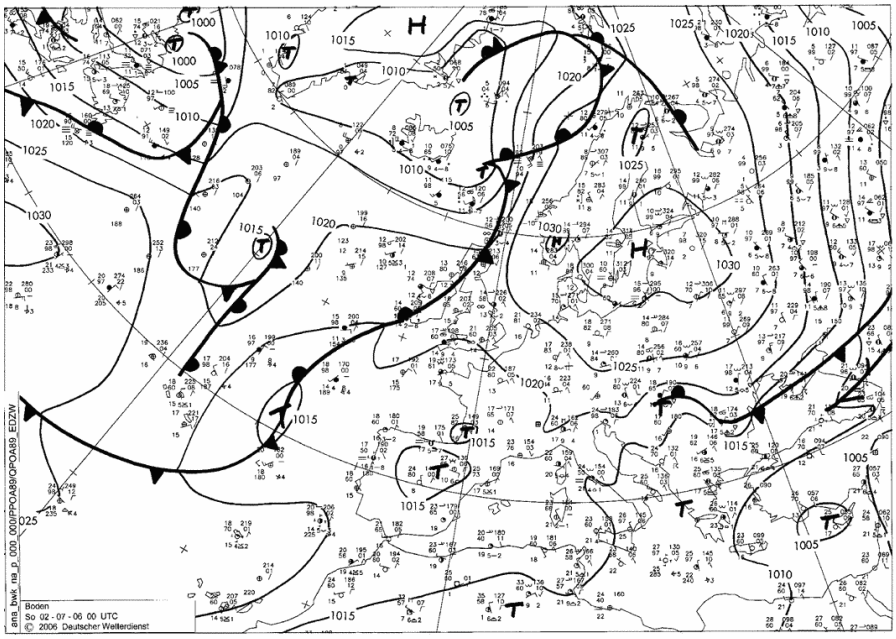

Figure 5.1: Surface analysis for July 2nd, 2006.

research (CESAR) is located. By looking at historical surface analysis charts in Figure 5.1 one notices that there is little change in the synoptic flow from July 1st to July 2nd. This lack of change throughout the period allowed consistent conditions to develop within the boundary layer. Also, there is a dominant high pressure system located over the Baltic Sea with effects reaching into the area of interest providing quiescent flow. Since high pressure systems are correlated with subsidence, clear skies were also observed with calm surface conditions. The CESAR field site is relatively flat. This location has a 200 meter tall meteorological tower that has been collecting observations involving wind speeds, wind direction, temperature and humidity at various heights for many decades [Bosveld et al., 2012]. The flat homogeneous landscape and quiet synoptic conditions lead to an observed LLJ developed by an IO.

5.3 Model set-up

The advanced research WRFv3.3 (ARW) released in April 2011 is the model of choice. The domain configuration (Figure 5.2) consisted of three domains with an inner high resolution 3km domain, middle 9km, and outer coarse 27km domain. 51 vertical levels are set with approximately 18 levels below 1000 meters. Each domains centerpoint was the location of CESAR in

Cabauw, The Netherlands where the observations from the GABLS3 study originated.

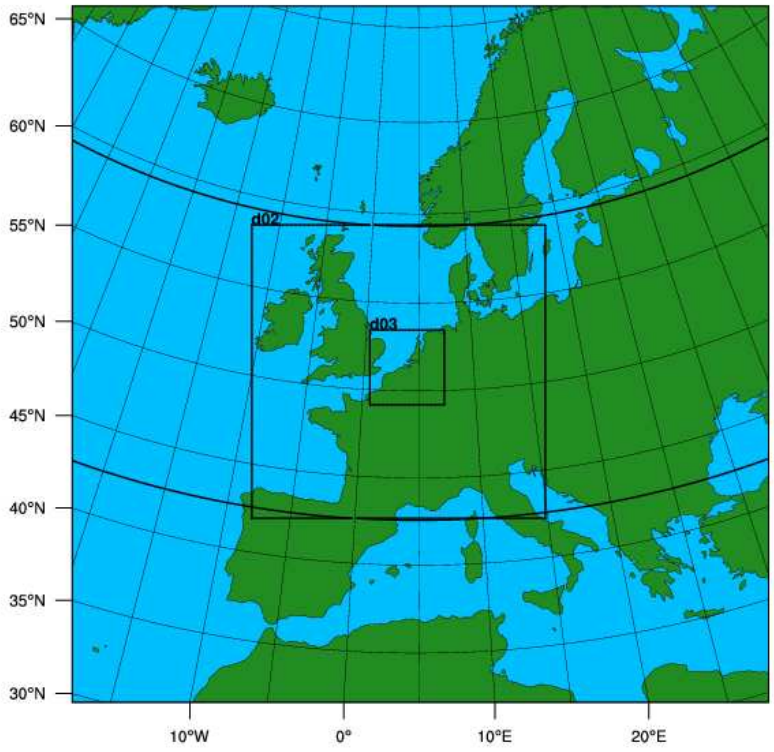

Figure 5.2: Model Domains. Horizontal grid resolutions: 27/9/3 km. Center of the entire domain is the approximate location of Cabauw, The Netherlands

Each simulation run involved a 48 hour simulation beginning at 12UTC June 30th and ending at 12UTC July 2nd in the year 2006. This time frame included a 36 hour spin up before the time period of interest 00UTC July 2nd through 09UTC July 2nd. The large spin up time was to ensure at least a full diurnal cycle was simulated before the time period of interest. Most of the data analyzed is from the central point of the innermost domain closest to that of CESAR with output every ten minutes to allow for a comprehensive understanding of the flow. The initial and boundary conditions were collected from the ERA-Interim (European Centre for Medium-range Weather Forecasts (ECMWF) reanalysis interim) dataset.

For this case study the model was run for a total of three times holding all parameterizations constant, except for specified changes in the YSU PBL scheme. The microphysics option was

the WRF single moment 5 class scheme (WSM5) [Hong et al., 2004], the Rapid Radiative Transfer model (RRTM) [Mlawer et al., 1997] for the longwave radiation scheme, the Dudhia shortwave radiation scheme [Dudhia, 1989], and the Noah land-surface model (LSM) [Chen and Dudhia, 2001]. For the cumulus scheme the Kain Fritsch (KF) [Kain, 2004] was chosen, but because the innermost domain had the capabilities of explicitly parameterizing cloud processes, the KF cumulus scheme was only used for the 27 km and 9 km resolution domains. The first of the three model runs consisted of the original YSU scheme Hong and Pan [1996], Hong et al. [2006] also known as YSU_0, the second model run consisted of bug fix (discussed in Chapter 4) and called as YSU_1, finally the third model run involved the addition of the new equation described in Chapter 3 and is called YSU_2.

5.4 Results

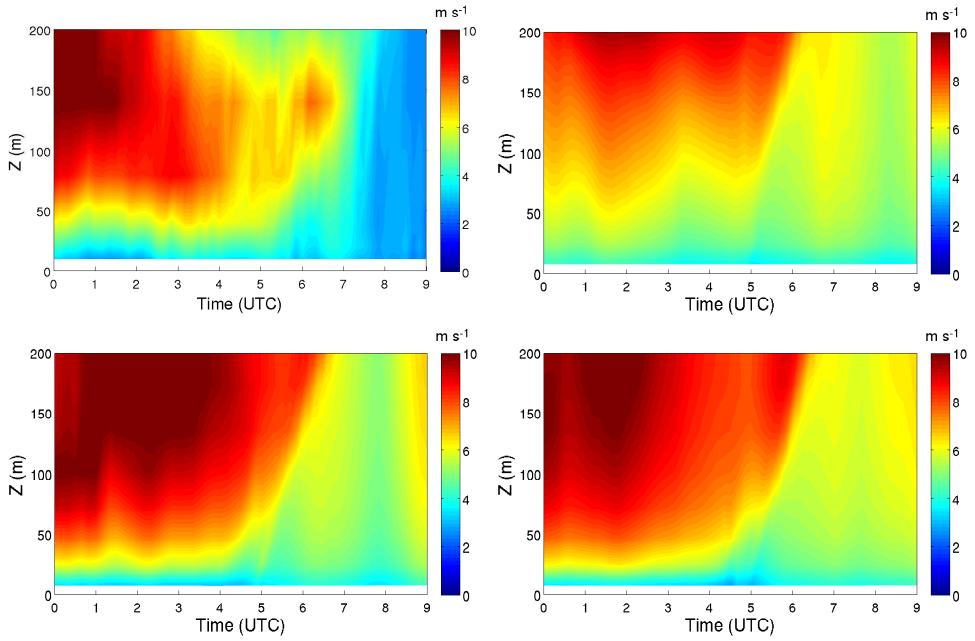

Figure 5.3: Time-height plots observed and simulated wind speed (m s^{-1}). Top left: Tower Observations. Top Right: YSU_0, Bottom left: YSU_1, Bottom right: YSU_2

Figure 5.3 shows the wind speed plots for the observations, original YSU, Modified YSU, and the NCSU YSU simulations. The tower observations reveal a LLJ with a core centered around 150 m above ground level with the effects of the extending over a 6 hour period. YSU_0

performed the worse developing the most diffused LLJ. Similar to previous findings, YSU_0 overestimated the LLJ height and underestimated the magnitude [Storm and Basu, 2010, Shin and Hong, 2011]. This enhanced diffusion from the 'bug' inside the code that was discussed in the previous chapter. The reasoning behind this is solidified when viewing the results from the YSU_1 run. The largest improvement is seen between YSU_0 and YSU_1 where the simulations went from extremely diffuse to developing a LLJ that overestimated the magnitude and matched the approximate observed LLJ-peak height. However, YSU_1 extended the extent of the LLJ features in time. The YSU_2 run with the added equation again improved the simulation by simulated the LLJ that matched closest to the observed LLJ for wind speeds.

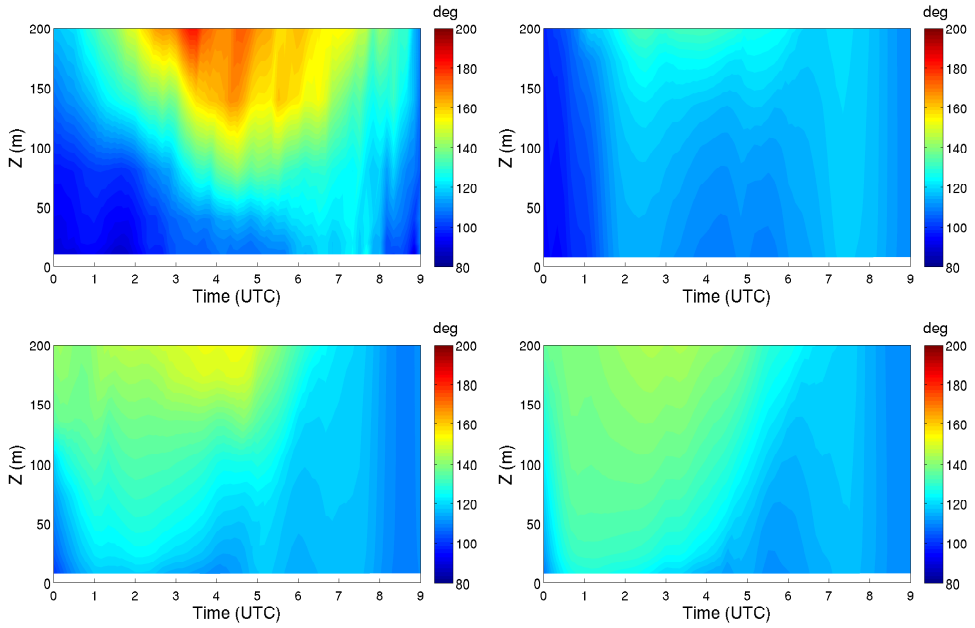

Figure 5.4: Time-height plots of observed and simulated wind direction. Top left: Tower Observations. Top Right: YSU_0, Bottom left: YSU_1, Bottom right: YSU_2

For the wind direction of tower observations and the three model simulations, refer to figure 5.4. The observations show significant change in wind direction in the vertical direction representing strong wind directional shear (magnitude of $\sim$ 80 over 200 m). The simulation utilizing the YSU_0 scheme does not produce significant directional wind shear; this is due to spurious enhanced mixing. Increasing diffusion decreases the vertical wind shear. Both the YSU_1 and YSU_2 schemes produce similar results by increasing directional wind shear by about 20 to 30 degrees in the vertical, especially between the hours of 00UTC and 04UTC. Although

both YSU_1 and YSU_2 unquestionably outperform the YSU_0 scheme, unfortunately they do not produce results matching what was observed.

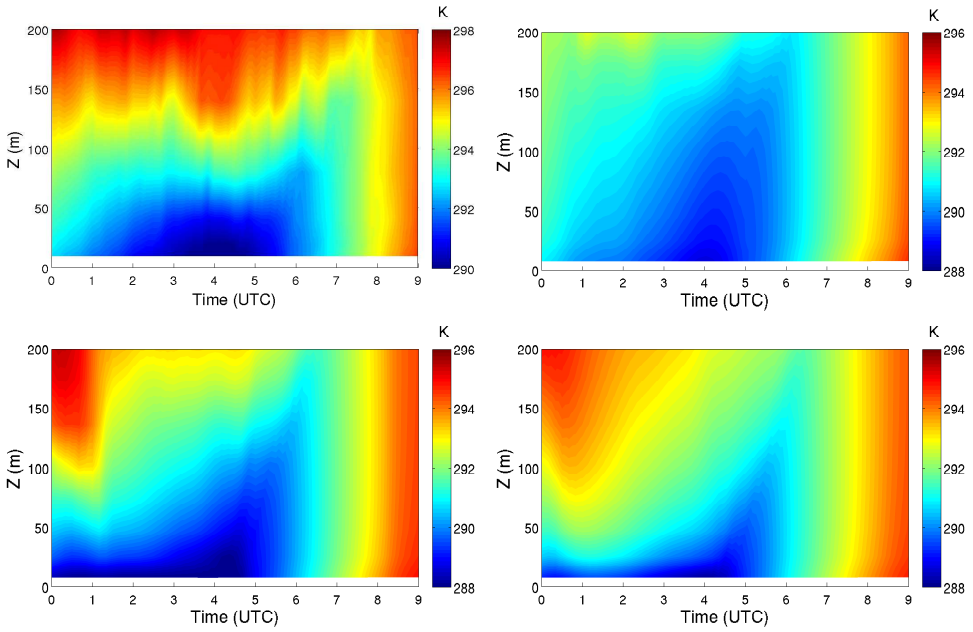

Figure 5.5: Time-height plots of observed and simulated potential temperature. Top left: Tower Observations. Top Right: YSU_0, Bottom left: YSU_1, Bottom right: YSU_2

The potential temperature values are plotted in figure 5.5 for tower observations and all three of the YSU simulations. At the first glance, all of the simulations underestimate the potential temperature values for the entire period. This is due likely due to the bias in the initial and boundary conditions. Because of this the simulation images have colorbars representing cooler values by a value of 2 K so overall PBL behavior could be compared with observations. With the enhanced diffusion YSU_0 simulated the coldest SBL. The YSU_1 simulation shows signs of improvement with a shallower surface inversion layer but the major improvement is with the YSU_2 simulation. With a more shallow surface inversion layer the YSU_2 simulation seems to reduce the diffusivity a bit more but is still far from observations.

Surface friction velocity (u_*) and sensible heat flux (HFX) time series values are plotted in figure 5.6. All of the simulations overestimate u_* values, especially during the later part of the time period for daytime hours. For the evening hours YSU_0 performed the worst overestimating u_*. This may be another direct result of the enhance diffusion causing larger values of u_* to develop. Similar to previously discussed results YSU_1 and YSU_2 performed similarly and closer

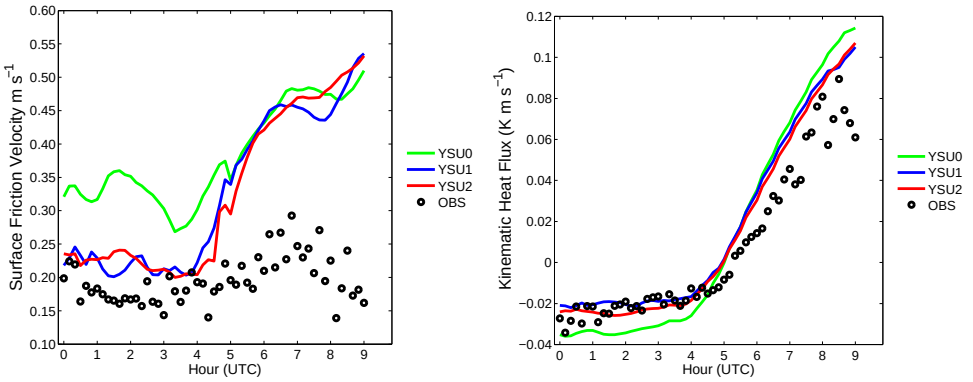

Figure 5.6: Time series plots of observed and simulated surface friction velocity (u_*) and sensible heat flux (HFX). left: u_*. Right: HFX. Observations are Black circles, YSU_0 is represented by the green line, YSU_1 blue, and YSU_2 was the red line.

to observations than YSU_0. When viewing the HFX results, at first glance the simulations look to have performed similarly to what was observed. However, again YSU_0 again performed farthest from the truth underestimating for the first half of the period and overestimating the second half of the period. YSU_1 was closer to observations but YSU_2 performed closest to the truth.

5.5 Conclusion

The major findings from this chapter give insight to the question on whether or not the YSU scheme could be improved. Realistic runs utilizing the WRF model for the GABLS3 case study revealed that a bug fix greatly improved the YSU PBL scheme. Enhanced diffusion was found to be the source causing YSU_0 to simulate LLJs with higher heights and lower magnitudes. The enhanced diffusion was found to occur within the eddy diffusivity equations for momentum and heat. Basically, the equations treated diffusion as if it was related to neutral stability. This enhanced diffusion in the wind speed values was greatly reduced from YSU_0 to YSU_1. However, strong mixing was still evident in the potential temperature plots for YSU_1. Implementing a new equation for a stability dependent critical Richardson number further decreased the enhanced diffusion remaining in the YSU_1 simulation. These improvements were more prominent in the potential temperature where mixing was visibly reduced. Although most of the differences are small between YSU_1 and YSU_2, this proves that the new relationship is working within the WRF model (at least for the GABLS3 case). Since YSU_2 is performing similar (slightly better) to YSU_1 the dynamic relationship shows to stay on course physically and is a better choice from physical standpoint. Theoretically, utilizing a dynamic (tuning-free) model is always a

better choice. However, more extreme cases will need to be tested to show the benefit of the newly purposed critical bulk Richardson number. Therefore, for the GABLS3 case study over Cabuaw, The Netherlands the YSU scheme could be improved. However, to deduce if this improvement will work for many different regimes more case studies will need to be analyzed.

Chapter 6

Future Directions

Based on the findings of this thesis, the following research avenues should be pursued:

- Even though the newly proposed Ri_{Bc} formulation is based on an extensive LES database, it does not cover the entire parameter space. More LES runs are needed to fill the voids in the existing LES database. The LES database should also contain realistic stable boundary layer flow fields generated by a coupled mesoscale-LES approach. These coupled simulations should include the effects of natural topography and land-surface heterogeneities, baroclinicity, large-scale advection, subsidence, interactions among several physical process, etc.

- Observational data from several field campaigns and wind tunnel experiments should be utilized to validate the proposed Ri_{Bc} formulation. The following field datasets are recommended: Cabauw, CASES97, CASES99, CBLAST, FLOSS, and Wangara. Wind tunnel observations by S. P. Arya and Y. Ohya could also be used.

- At present, the proposed Ri_{Bc} formulation does not have a strong theoretical foundation. It is qualitatively similar to the empirical formulation (based on resistance laws) by Melgarejo and Deardorff [1974]. An attempt should be made to derive the proposed formulation using the well-established local scaling hypothesis.

- The proposed Ri_{Bc} formulation is only valid for stable boundary layer flows. It should be extended to convective boundary layer cases in the near future.

- In the present thesis, the exponent p in the K-profile approach is assumed to be equal to 2. This value is also assumed by most of the NWP models. However, to the best of our knowledge, no systematic study has been conducted to characterize the properties of p. Troen and Mahrt [1986] speculated that p could be a function of stability. Rigorous analyses of observed and LES-generated data are recommended to address this issue.

- Following the YSU PBL scheme, K_h is assumed to be equal to K_m in this thesis. However, a handful of studies (e.g., Kim and Mahrt [1992]) suggested that the Prandtl number, $Pr_T(= K_m/K_h)$, is dependent on stability. Given the theoretical and practical significance of the Prandtl number, this unsettled topic should be revisited.

- More idealized single column modeling studies should be performed utilizing the K-profile method in conjunction with the newly proposed Ri_{Bc} formulation (i.e., YSU2 scheme). The simulated results should be compared with LES results, as well as other popular PBL schemes (e.g., MYJ scheme, Louis-Tiedtke-Geleyn scheme).

- Perform rigorous, multi-month, multi-region model validation studies utilizing the YSU1 and YSU2 PBL schemes. Towards this end, a series of WRF model runs for the month of July in 2011 was recently conducted. The model setup consists of three domains with 27, 9, and 3 km resolutions with a center location over Lubbock, TX. Figure 6.1 shows the future domain setup for what will be referred to as the Texas runs. The namelist options are the same as those that were used during the GABLS3 case study (see Chapter 5). For the initialization dataset the NCEP/NCAR reanalysis data (NNRP) is utilized.

  This location is chosen due to the availability of observations for future analysis from a sonic detection and ranging (SODAR) instrument and a 200 m meteorological tower. The SODAR is provided and placed in Lubbock, TX by North Carolina State University (NCSU) with a 5 m resolution averaging the wind speed every ten minutes. Texas Tech University (TTU) provided the observations from the 200 m Tower instrumented at 10 levels with sonic anemometers and other sensors.

  Each run consists of a 36 hour run with a 12 hour spin up time before the 24 hour time period of interest. For example, July 1st, 2011 was initialized on June 30th, 2011 12UTC and ran through to July 2nd, 2011 00UTC. These runs were placed online for a side to side comparison with observations at http://www4.ncsu.edu/~sbasu5/LLJ . This extended time period allows a more thorough analysis to take place increasing/decreasing confidence that the modifications will improve the performance of the YSU PBL scheme. Three case studies are shown below as illustrative examples.

  The case studies which are extracted from the website are July 16, 21 and 22 in the year 2011 (figures 6.2, 6.3 and 6.4). For July 21 and 22 the wind speed values simulated for both YSU_1 and YSU_2 produced very similar results in comparison with each other and produced LLJs at approximately the observed heights. However, their simulated magnitudes were about 2 m s^{-1} lower. Similar to what was mentioned in the above chapters the two schemes probably performed very similar in that these cases may have resulted in $Ri_{Bc]}$ at or around 0.25. Although most of the July models simulations were

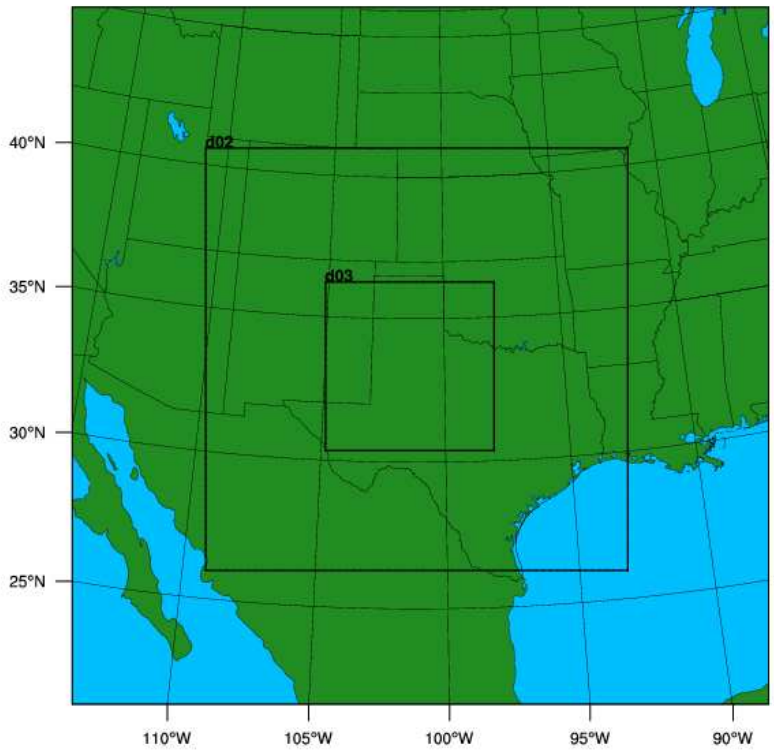

Figure 6.1: Model Domains. Horizontal grid resolutions: 27/9/3 km. Center of the entire domain is the approximate location of Lubbock, TX

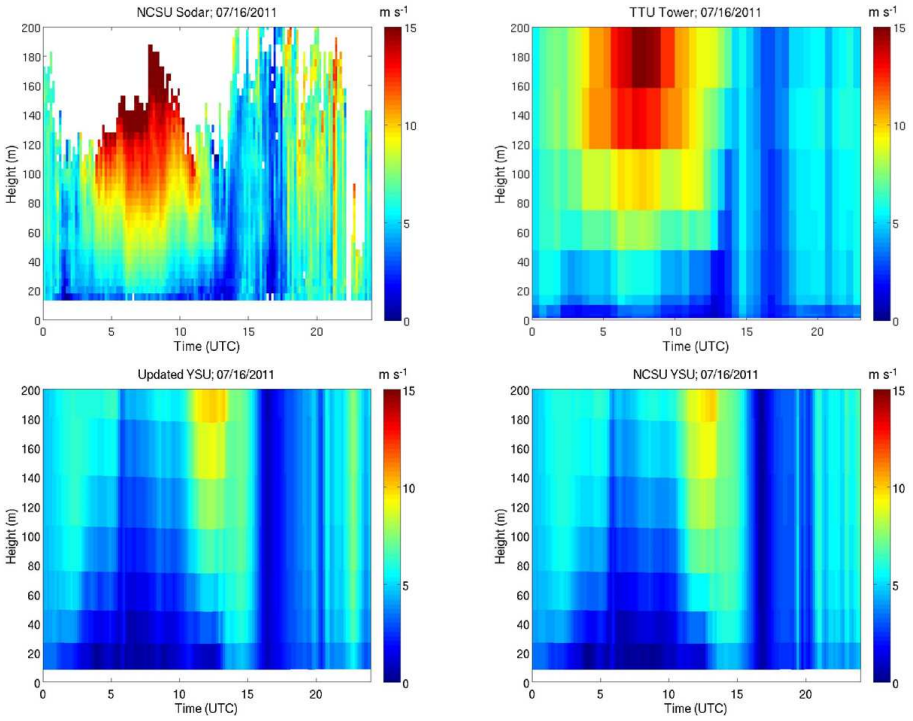

Figure 6.2: Time-height plots of observed and simulated total wind speed for July 16, 2011. Top left: NCSU Sodar Observations. Top Right: TTU Tower observations, Bottom left: YSU_1, Bottom right: YSU_2

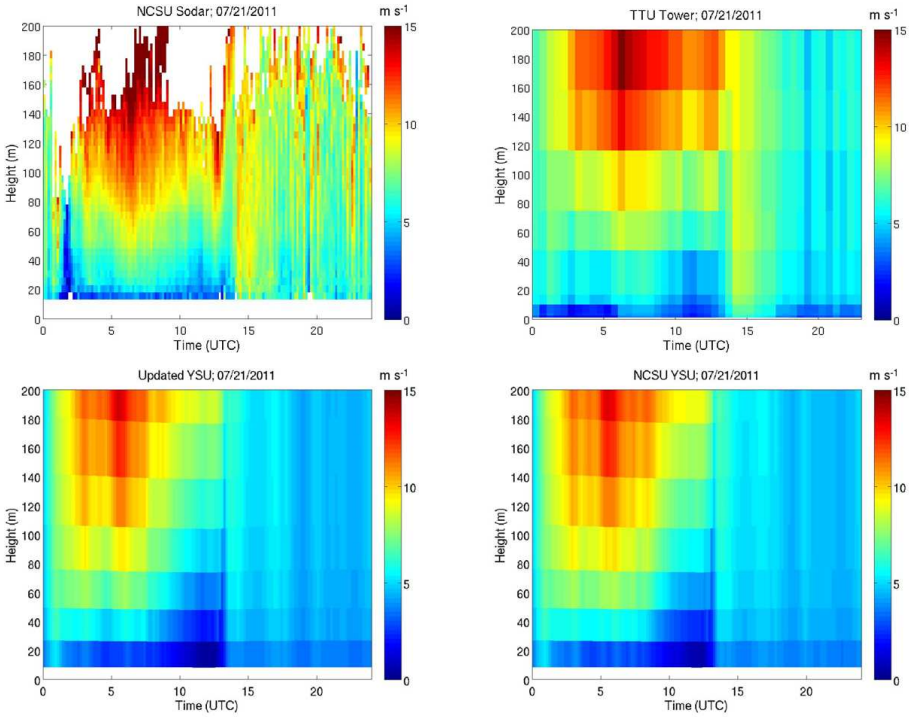

Figure 6.3: Time-height plots of observed and simulated total wind speed for July 21, 2011. Top left: NCSU Sodar Observations. Top Right: TTU Tower observations, Bottom left: YSU_1, Bottom right: YSU_2

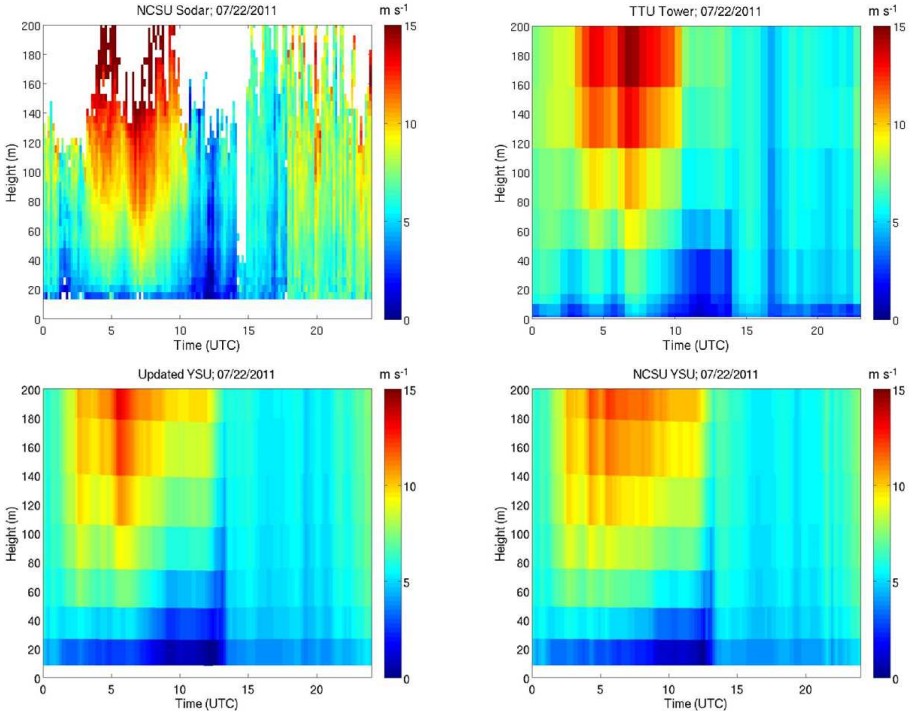

Figure 6.4: Time-height plots of observed and simulated total wind speed for July 22, 2011. Top left: NCSU Sodar Observations. Top Right: TTU Tower observations, Bottom left: YSU_1, Bottom right: YSU_2

in similar caliber to the 21 and 22, the day of July 16 shows that there may be situations where this may not be the case. July 16 contained an observed LLJ with a core occurring around 150 m above ground level with magnitudes around 15 m s^{-1}. The YSU_1 and YSU_2 simulations, unfortunately, did not produce anything that could be considered an LLJ. It is because of results like this that perpetuate the constant battle on improving PBL schemes as the science of today cannot create a scheme capable of working for all weather environments.

REFERENCES

W. C. Anderson, S. Basu, and C. W. Letchford. Comparison of dynamic subgrid-scale models for simulations of neutrally buoyant shear-driven atmospheric boundary layer flows. Environ. Fluid Mech., 7:195–215, 2007.

E. L. Andreas, K. J. Claffey, and A. P. Makshtas. Low-level atmospheric jets ad inversions over the western Weddell sea. Boundary-Layer Meteorol., 97:459–486, 2000.

R. M. Banta, R. K. Newsom, J. K. Lundquist, Y. L. Pichugina, R. L. Coulter, and L. Mahrt. Nocturnal low-level jet characteristics over Kansas during CASES-99. Boundary-Layer Meteorol., 105:221–252, 2002.

S. Basu and F. Porté-Agel. Large-eddy simulation of stably stratified atmospheric boundary layer turbulence: A scale-dependent dynamic modeling approach. J. Atmos. Sci., 63:2074–2091, 2006.

S. Basu, F. Porté-Agel, E. Foufoula-Georgiou, J.-F. Vinuesa, and M. Pahlow. Revisiting the local scaling hypothesis in stably stratified atmospheric boundary layer turbulence: an integration of field and laboratory measurements with large-eddy simulations. Boundary-Layer Meteorol., 119:473–500, 2006.

S. Basu, A. A. M. Holtslag, B. J. H. van de Wiel, A. F. Moene, and G.-J. Steeneveld. An inconvenient "truth" about using sensible heat flux as a surface boundary condition in models under stably stratified regimes. Acta Geophysica, 56:88–99, 2008a.

S. Basu, J.-F. Vinuesa, and A. Swift. Dynamic LES modeling of a diurnal cycle. J. Appl. Meteorol. Climatol., 47:1156–1174, 2008b.

S. Basu, A. A. M. Holtslag, and F. C. Bosveld. GABLS3 LES intercomparison study. In ECMWF/GABLS Workshop on "Diurnal cycles and the stable atmospheric boundary layer", pages 75–82, ECMWF, 2011.

R. J. Beare, M. K. Macvean, A. A. M. Holtslag, J. Cuxart, I. Esau, J.-C. Golaz, M. A. Jimenez, M. Khairoutkinov, B. Kosovic, D. Lewellen, T. S. Lund, J. K. Lundquist, A. Mccabe, A. F. Moene, Y. Noh, S. Raasch, and P. Sullivan. An intercomparison of large-eddy simulations of the stable boundary layer. Bound. Layer Meteor., 118:247–272, 2006.

A. Beljaars and P. Viterbo. The role of the boundary layer in a numerical weather prediction model. In A. A. M. Holtslag and P. G. Duynkerke, editors, Clear and Cloudy Boundary Layers, pages 297–304. Royal Netherlands Academy of Arts and Sciences, Amsterdam, 1998.

A. Blackadar. Boundary layer wind maxima and their significance for the growth of nocturnal inversions. Bull. Amer. Meteor. Soc., 38:283–290, 1957.

F. C. Bosveld, E. V. Meijgaard, E. I. F. D. Bruijn, G.-J. Steeneveld, and A. A. M. Holtslag. The gabls third intercomparison case for model evaluation: Case selection and set-up. under review, 2012.

R. A. Brost and J. C. Wyngaard. A model study of the stably stratified planetary boundary layer. J. Atmos. Sci., 35:1427–1440, 1978.

A. R. Brown, S. H. Derbyshire, and P. J. Mason. Large-eddy simulation of stable atmospheric boundary layers with a revised stochastic subgrid model. Quart. J. Roy. Meteor. Soc., 120: 1485–1512, 1994.

J. A. Businger, J. C. Wyngaard, Y. Izumi, and E. F. Bradley. Flux-profile relationships in the atmospheric surface layer. J. Atmos. Sci., 28:181–189, 1971.

F. Chen and J. Dudhia. Coupling an advanced land-surface/ hydrology model with the penn state/ ncar mm5 modeling system. part i: Model description and implementation. Mon. Wea. Rev., 129:569–585, 2001.

R. H. Clarke, A. J. Dyer, R. R. Brook, D. G. Reid, and A. J. Troup. The Wangara experiment: boundary layer data Tech. Paper No. 19. CSIRO, Div. Meteor. Phys. Aspendale, Australia, 1971. 362 pp.

J. Cuxart, A. A. M. Holtslag, R. J. Beare, E. Bazile, A. Beljaars, A. Cheng, L. Conangla, M. EK, F. Freedman, R. Hamdi, A. Kerstein, H. Kitagawa, G. Lenderink, D. Lewellen, J. Mailhot, T. Mauritsen, V. Perov, G. Schayes, S. G-J, G. Svensson, P. Taylor, W. Weng, S. Wunsch, and K.-M. XU. Single-column model intercomparison for a stably stratified atmospheric boundary layer. Bound. Layer Meteor., 118:273–303, 2006.

DOE. 20% wind energy by 2030: Increasing wind energy's contribution to U.S. electric supply. Technical report, U.S. Department of Energy, 2008.

J. Dudhia. Numerical study of convection observed during the winter monsoon experiment using a mesoscale two-dimensional model. J. Atmos. Sci., 46:3077–3107, 1989.

I. Esau and S. Zilitinkevich. On the role of the planetary boundary layer depth in the climate system. Adv. Sci. Res., 4:63–69, 2010.

I. N. Esau and S. S. Zilitinkevich. Universal dependences between turbulent and mean flow parameters instably and neutrally stratified planetary boundary layers. Nonlin. Processes Geophys., 13:135–144, 2006.

J. A. García, M. L. Cancillo, and J. L. Cano. A case study of the morning evolution of the convective boundary layer depth. J. Appl. Meteorol., 41:1053–1059, 2002.

J. R. Garratt. The atmospheric boundary layer. Cambridge University Press, Cambridge, UK, 1992.

S.-E. Gryning and E. Batchvarova. Marine atmospheric boundary-layer height estimated from NWP model output. Int. J. Environ. Poll., 20:147–153, 2003.

S. R. Hanna. The thickness of the planetary boundary layer. Atmos. Environ., 3:519–536, 1969.

G. Heinemann and L. Rose. Surface energy balance, parameterizations of boundary-layer heights and the application of resistance laws near an antarctic ice shelf front. Boundary-Layer Meteorol., 51:123–158, 1990.

J. Holton. The dirunal boundary layer wind oscillation above sloping terrain. Tellus, 19:573–583, 1967.

A. A. M. Holtslag and B. A. Boville. Local versus nonlocal boundary-layer diffusion in a global climate model. J. Climate, 6:1825–1842, 1993.

A. A. M. Holtslag, E. I. F. de Bruijn, and H.-L. Pan. A high resolution air mass transformation model for short-range weather forecasting. Mon. Wea. Rev., 118:1561–1575, 1990.

A. A. M. Holtslag, G.-J. Steeneveld, and v. B. J. H. Role of land surface temperature feedback on model performance for stable boundary layers. Boundary-Layer Meteorol., 125:361–376, 2007.

S.-Y. Hong. A new stable boundary-layer mixing scheme and its impact on the simulated east asian summer monsoon. Q. J. R. Meteorol. Soc., 136:1481–1496, 2010.

S.-Y. Hong and H.-L. Pan. Nonlocal boundary layer vertical diffusion in a medium-range forecast model. Mon. Wea. Rev., 124:2322–2339, 1996.

S.-Y. Hong, J. Dudhia, and S.-H. Chen. A revised approach to ice microphysical processes for the bulk parameterization of clouds and precipitation. Mon. Wea. Rev., 132:103–120, 2004.

S.-Y. Hong, Y. Noh, and J. Dudhia. A new vertical diffusion package with an explicit treatment of entrainment processes. Mon. Wea. Rev., 134:2318–2341, 2006.

A. Jeričević and B. Grisogono. The critical bulk Richardson number in urban areas: verification and application in numerical weather prediction model. Tellus, 58A:19–27, 2006.

M. A. Jiménez and J. Cuxart. Large-eddy simulations of the stable boundary layer using the standard kolmogorov theory: Range of applicability. Boundary-Layer Meteor., 115:241–261, 2005.

J. Kain. The kain-fritsch convective parameterization: An update. J. Appl. Meteor., 43:170–181, 2004.

N. D. Kelley, M. Shirazi, S. W. D. Jager, P. Sullivan, and E. Patton. Lamar low-level jet project interim report. Technical report, Tech. Rep. NREL/TP-500-34593, National Renewable Energy Laboratory, 2004.

J. Kim and L. Mahrt. Simple formulation of turbulent mixing in the stable free atmosphere and nocturnal boundary layer. Tellus, 44A:381–394, 1992.

L. Mahrt. Modelling the depth of the stable boundary-layer. Boundary-Layer Meteorol., 21: 3–19, 1981.

J. W. Melgarejo and J. W. Deardorff. Stability functions for the boundary-layer resistance laws based upon observed boundary-layer heights. J. Atmos. Sci., 31:1324–1333, 1974.

E. Mlawer, S. Taubman, P. Brown, M. Iacono, and S. Clough. Radiative transfer for inhomogeneous atmosphere: Rrtm, a validated correlated-k model for the longwave. J. Geophys. Res., 102:16663–16682, 1997.

F. T. M. Nieuwstadt. The turbulent structure of the stable, nocturnal boundary layer. J. Atmos. Sci., 41:2202–2216, 1984.

J. J. O'Brien. A note on the vertical structure of the eddy echange coefficient in the planetary boundary layer. J. Atmos. Sci., 27:1213–1215, 1970.

T. R. Parish and L. D. Oolman. On the role of sloping terrain in the forcing of the great plains low-level jet. J. Atmos. Sci., 67:2690–2699, 2011.

J. E. Pleim. A combined local and nonlocal closure model for the atmospheric boundary layer. part i: model description and testing. J. Appl. Meteor. Climatol., 46:1383–1395, 2007a.

J. E. Pleim. A combined local and nonlocal closure model for the atmospheric boundary layer. part ii: Application and evaluation in a mesoscale meteorological model. J. Appl. Meteor. Climatol., 46:1396–1409, 2007b.

H. Richardson, Y. Wang, and S. Basu. Low-level jets - the lifeblood of wind energy. Can we simulate and forecast them with high fidelity? In Euromech Colloquium 528 on Wind Energy and the impact of turbulence on the conversion process, Oldenburg, Germany, 2012.

D. Rife, J. Pinto, A. Monaghan, C. Davis, and J. Hannan. H13-219 corridors of enhanced transport and dispersion: Global distribution and characteristics. In 13th Conference on Harmonisation within Atmoshperic Modelling for Regulatory Purposes, Paris, France, 2010.

H. Russett and S. Basu. Simulations of nocturnal low-level jets using the WRF model. In 12th Annual WRF Users' Workshop, Boulder, CO, USA, 2011.

E. M. Saiki, C.-H. Moeng, and P. P. Sullivan. Large-eddy simulation of the stably stratified planetary boundary layer. Boundary-Layer Meteorol., 95:1–30, 2000.

P. Seibert, F. Beyrich, S.-E. Gryning, S. Joffre, A. Rasmussen, and P. Tercier. Mixing height determination for dispersion modelling, 1998.

H. H. Shin and S. Hong. Intercomparison of planetary boundary-layer parameterizations in the WRF model for a single day from CASES-99. Boundary-Layer Meteor., 139:261–281, 2011.

Z. Sorbjan. Structure of Atmospheric Boundary Layer. Prentice-Hall, Englewood Cliffs, NJ, 1989. 317 pp.

J. H. Sørensen, A. Rasmussen, and H. Svensmark. Forecast of atmospheric boundary-layer height utilised for ETEX real-time dispersion modelling. Phys. Chem. Earth., 21:435–439, 1996.

D. J. Stensrud. Parameterization Schemes, Keys to Understanding Numberical Weather Prediction Models. Cambridge University Press, Cambridge, UK, 2007.

B. Storm and S. Basu. The WRF model forecast-derived low-level wind shear climatology over the United States Great Plains. Energies, 3:258–276, 2010.

R. B. Stull. An Introduction to Boundary Layer Meteorology, volume 13. Springer, 1988a.

R. B. Stull. An Introduction to Boundary Layer Meteorology. Kluwer Academic Publishers, Dordrecht, The Netherlands, 1988b. 670 pp.

S. Sukoriansky, B. Galperin, and V. Perov. Application of a new spectral theory of stably stratified turbulence to the atmospheric boundary layer over sea ice. Bound. Layer Meteor., 117:231–257, 2005.

I. Troen and L. Mahrt. A simple model of the atmospheric boundary layer; sensitvity to surface evaporation. Boundary-Layer Meteorol., 37:129–148, 1986.

L. Uccellini and D. Johnson. The coupling of upper and lower tropospheric jet streams and implications for the development of severe convective storms. Mon. Wea. Rev., 107:682–703, 1979.

B. J. H. van de Wiel, A. F. Moene, G. J. Steeneveld, P. Baas, and F. C. Bosveld. A conceptual view on inertial oscillations and nocturnal low-level jets. J. Atmos. Sci., 67:2679–2689, 2010.

D. Vickers and L. Mahrt. Evaluating formulations of stable boundary layer height. J. Appl. Meteorol., 43:1736–1749, 2004.

J.-F. Vinuesa, S. Basu, and S. Galmarini. The diurnal evolution of ^{222}Rn and its progeny in the atmospheric boundary layer during the Wangara experiment. Atmos. Chem. Phys., 7: 5003–5019, 2007.

D. H. P. Vogelezang and A. A. M. Holtslag. Evaluation and model impacts of alternative boundary-layer height formulations. Boundary-Layer Meteorol., 81:245–269, 1996.

H. Wexler. A boundary layer interpretation of the low level jet. Tellus, 13:368–378, 1961.

T. Yamada. On the similarity functions A, B and C of the planetary boundary layer. J. Atmos. Sci., 33:781–793, 1976.

S. Zilitinkevich and A. Baklanov. Calculation of the height of the stable boundary layer in practical applications. Boundary-Layer Meteorol., 105:389–409, 2002.

APPENDICES

Appendix A

Background Derivations

A.1 Blackadar's Derivation

In order to allow for a simplified derivation Blackadar assumed friction goes to zero when the Sun sets leaving equations 2.1 and 2.2 to become the next set of equations.

$$\frac{\partial U}{\partial t} = fV \tag{A.1}$$

$$\frac{\partial V}{\partial t} = f(G - U) \tag{A.2}$$

From here the derivative of equations A.1 and A.2 are taken resulting in the following.

$$\frac{\partial^2 U}{\partial t^2} = f\frac{\partial V}{\partial t} \tag{A.3}$$

$$\frac{\partial^2 V}{\partial t^2} = -f\frac{\partial U}{\partial t} \tag{A.4}$$

Plugging equation A.2 into A.3 and A.1 into A.4 and multiplying both sets by the Coriolis parameter lead to

$$\frac{\partial^2 U}{\partial t^2} = f^2(G - U) \tag{A.5}$$

$$-\frac{\partial^2 V}{\partial t^2} = f^2 V \tag{A.6}$$

By distributing the Coriolis parameter in equation A.5 and subtracting each term by the geostrophic parameter (G), where $\phi = U - G$, equation A.5 became

$$\frac{\partial^2 \phi}{\partial t^2} + f^2(\phi) = 0 \tag{A.7}$$

and by some algebra A.6 became the following.

$$\frac{\partial^2 V}{\partial t^2} + f^2 V = 0 \tag{A.8}$$

By solving the partial differential equations and utilizing the initial conditions of the IO where $U = U_o, V = V_o$ at $t = 0$ Blackadar's governing equaitons for the IO read:

$$U - G = V_o sin(ft) + (U_o - G)cos(ft) \tag{A.9}$$

$$V = V_o cos(ft) - (U_o - G)sin(ft) \tag{A.10}$$

A.2 Van de Weil et al.'s Derivation

Using shorthand notiation for the turbulence stress terms $F_x(z,t) = \frac{\partial \frac{\tau_x}{\rho}}{\partial z}$ and $F_y(z,t) = \frac{\partial \frac{\tau_y}{\rho}}{\partial z}$ and while in an equilibrium state $F_x(z,t) = F_{xeq}(z)$ and $F_y(z,t) = F_{yeq}(z)$. By plugging these terms into the stationary state equations of 2.1 and 2.2 the following was found:

$$0 = fV_{eq} + F_{xeq}(z) \tag{A.11}$$

$$0 = f(G - U_{eq}) + F_{yeq}(z) \tag{A.12}$$

By subtracting both equations by their stress terms and plugging them into 2.1 and 2.2 and after some algebra the following was found [van de Wiel et al., 2010]:

$$\frac{\partial U - U_{eq}}{\partial t} = f(V - V_{eq}) \tag{A.13}$$

$$\frac{\partial V - V_{eq}}{\partial t} = -f(U - U_{eq}) \tag{A.14}$$

Following the similar procedure as before for an undamped solution the new governing equations were found to be:

$$U - U_{eq} = (V_o - V_{eq})sin(ft) + (U_o - U_{eq})cos(ft) \tag{A.15}$$

$$V - V_{eq} = (V_o - V_{eq})cos(ft) - (U_o - U_{eq})sin(ft) \tag{A.16}$$

Where U_{eq} and V_{eq} represent the equilibrium values present if friction remained after evening transition and U_o and V_o are the values at $t = 0$.

Appendix B

B.1 Neutral K_m Derivation

The log-law starts with knowing that the flux is proportional to the gradient. Therefore the following equation was developed:

$$\overline{u'w'} = -K_m \frac{\partial \bar{u}}{\partial z} \tag{B.1}$$

From here $\overline{u'w'} = -u_*^2$ leading equation B.1 to

$$-u_*^2 = -K_m \frac{\partial \bar{u}}{\partial z} \tag{B.2}$$

or,

$$K_m \frac{\partial \bar{u}}{\partial z} = u_*^2 \tag{B.3}$$

Utilizing the surface layer equation $K_m = kzu_*$ and plugging into B.3 the following was obtained

$$kzu_* \frac{\partial \bar{u}}{\partial z} = u_*^2 \tag{B.4}$$

or,

$$\frac{\partial \bar{u}}{\partial z} = \frac{u_*}{kz} \tag{B.5}$$

By taking the integral of both sides of the equation

$$\int_0^u d\bar{u} = \frac{u_*}{k} \int_{z_o}^z \frac{dz}{z} \tag{B.6}$$

therefore resulting in the log-law,

$$u = \frac{u_*}{k} ln\left(\frac{z}{z_o}\right) \tag{B.7}$$